F. C. Correia, J. M. Ribeiro, A. Kuzmin, I. Pudza, A. Kalinko, E. Welter, A. Mendes, J. Rodrigues, N. Ben Sedrine, T. Monteiro, M. R. Correia, C. J. Tavares, The role of Ga and Bi doping on the local structure of transparent zinc oxide thin films, J. Alloys Compd. 870 (2021) 159489.
Doi: 10.1016/j.jallcom.2021.159489.

The role of Ga and Bi doping on the local structure of transparent zinc oxide thin films

Filipe C. Correia[1], Joana M. Ribeiro[1], Alexei Kuzmin[2], Inga Pudza[2], Aleksandr Kalinko[3,4], Edmund Welter[4], Adelio Mendes[5], Joana Rodrigues[6], Nabiha Ben Sedrine[6], Teresa Monteiro[6], Maria Rosário Correia[6], Carlos J. Tavares[1]*

[1]Centre of Physics, University of Minho, 4710-057 Braga, Portugal

[2]Institute of Solid State Physics, University of Latvia, LV-1063 Riga, Latvia

[3]Department Chemie, Naturwissenschaftliche Fakultät, Universität Paderborn, Warburger Strasse 100, 33098 Paderborn, Germany

[4]Deutsches Elektronen-Synchrotron − A Research Centre of the Helmholtz Association, Notkestraße 85, D-22607 Hamburg, Germany

[5]LEPABE, Faculty of Engineering of the University of Porto, Rua Roberto Frias s/n, 4200-465 Porto, Portugal

[6]Departamento de Física & i3N, Universidade de Aveiro, 3810-193 Aveiro, Portugal

*Corresponding author: ctavares@fisica.uminho.pt; Telephone: +351 235 510474

Abstract

Transparent undoped ZnO and additionally doped with Ga and Bi thin films were produced by magnetron sputtering. The thin films were comprehensively characterized by X-ray absorption, X-ray diffraction (XRD), X-ray photoelectron spectroscopy (XPS), transmission and scanning transmission electron (TEM, STEM) microscopy and Raman spectroscopy. All undoped and doped films crystallise in a ZnO phase with the hexagonal wurtzite crystal structure. The local structure of the thin films was investigated by temperature-dependent X-ray absorption spectroscopy at the Zn and Ga K-edges, as well as at the Bi L_3-edge. It was found that the doping of Ga^{3+} and Bi^{3+} ions in the ZnO wurtzite structure produces distinct effects on the thin film microstructure. The substitution of Zn^{2+} ions by smaller Ga^{3+} ions introduces a static disorder to the thin film structure, which is evidenced by an increase in the mean-square relative displacements σ^2(Zn-O) and σ^2(Zn-Zn). At the same time, large Bi^{3+} ions do not substitute zinc ions, but are likely located in the disordered environment at the ZnO grain boundaries. This conclusion was directly supported by energy-dispersive X-ray spectroscopy combined with TEM and STEM observations as well as by resonant and non-resonant μ-Raman experiments at room temperature, where the ZnO and ZnO:Bi spectra are similar, suggesting a lack of structural disorder in the wurtzite cell. On the other hand, the Raman disorder-activated phonon is pronounced for Ga-doping of the ZnO lattice, confirming the compositional disorder. Both XRD and XPS ruled out Ga_2O_3 phases in Ga-doped ZnO; conversely, Bi_2O_3 and a small amount of Bi-metal phases are clearly discerned by XPS experiments, further suggesting that Bi is not incorporated in the ZnO wurtzite cell, but segregated to grain boundaries.

Keywords: Zinc oxide, thin films, sputtering, thermoelectric, X-ray absorption spectroscopy, Raman spectroscopy

1. Introduction

Zinc oxide (ZnO) is a direct band-gap semiconductor (~3.4 eV, at room temperature (RT)) well known for its applications in photodetectors, light-emitting diodes, photovoltaics, gas sensing and thin-film transistors [1–6], amongst other applications. ZnO thin films are commonly deposited by pulsed laser deposition, molecular beam epitaxy, atomic layer deposition, chemical synthesis and magnetron sputtering [7–9]. One of the most interesting applications of ZnO is for thermal energy harvesting, in the form of transparent thermoelectric thin films [10–13]. ZnO crystallizes in the hexagonal wurtzite structure and displays an intrinsic n-type conductivity that can be further enhanced to lower the electrical resistivity for use in optoelectronic devices. Typically, as in all undoped semiconductors at RT, ZnO thin films have a high electrical resistivity due to a low carrier concentration (~10^{16}-10^{17} cm^{-3}) [2,14]. Hence, it is most common to improve the ZnO electrical properties by doping, especially with elements of the III-B group (Ga, Al). In particular, the thermoelectric properties of ZnO can be affected by doping with Al^{3+}, Ga^{3+}, Bi^{3+} and other ions [13,15,16]. Since Bi^{3+} is a heavier ion with a very large ionic radius (1.03 Å), in comparison with Zn^{2+} (0.60 Å), the addition of bismuth to ZnO was proposed in several works [11–14] to modify its properties by creating thermal phonon scattering centres in the lattice. Thereby, one could expect a decrease in the thermal conductivity and, subsequently, an enhancement in the thermoelectric figure of merit, as in the case of Nb-doping in TiO_2, as reported elsewhere by the authors [17]. However, while the effect of Bi doping on the ZnO properties has been observed in [11–14], the way how bismuth ions are incorporated into the oxide matrix is still unclear.

Information on the atomic environment of ZnO:Ga,Bi thin films is scarce or non-existent in the literature. In particular, it has been challenging to discriminate between point defects (oxygen vacancies and Zn interstitials) and unintentional impurity doping. Hence, an in-depth study on the local order in these films was endured using highly sensitive characterization techniques such as temperature-dependent X-ray absorption spectroscopy, X-ray photoelectron spectroscopy, high-resolution electron microscopy, X-ray diffraction and Raman spectroscopy. The electric and thermoelectric properties of these ZnO:Ga,Bi thin films have been published elsewhere [13]. Hereafter, the focus of this manuscript is on the atomic environment and structural information, indispensable for the comprehension of the inherent and desired thermal transport and thermoelectric properties.

2. Experimental and data analysis

Undoped zinc oxide (ZnO) thin films and doped with Ga and Bi were prepared by magnetron sputtering. A confocal geometry was used with two circular magnetrons (10 cm diameter) in a home-made d.c. magnetron sputtering system. A 99.95% purity bismuth target was used for Bi doping (FHR Anlagenbau GmbH), while for the base ZnO films undoped and intrinsically doped ZnO targets were used: for ZnO, 99.95% purity; for ZnO:Ga, ZnO(95.5)Ga_2O_3(4.5)wt.%, 99.95% purity; FHR Anlagenbau GmbH. These films were deposited on 10 mm × 10 mm Si substrates with <100> orientation (SIEGERT WAFER GmbH, Part-No: L14016) and 10 mm × 10 mm Kapton® film. All substrates were previously cleaned with isopropanol in an ultrasound bath for 15 minutes. Prior to

deposition, the substrates were etched in an Ar^+ plasma at 2 Pa to further clean the exposed surfaces. The samples were fixed to a sample holder in the middle of the chamber with Kapton tape, radially symmetrical to the centre of the sample holder, fixed at 9 cm (vertically) from the normal to the centre of the targets, in a spinning platform to assure a homogeneous deposition. Several parameters were kept constant throughout all depositions, such as deposition time (20 min), current density on the intrinsically doped targets (5.0 $mA \cdot cm^{-2}$), substrate rotation speed (18 r.p.m), deposition temperature (200 ºC), argon flow (40 sccm), which corresponds to a working pressure of 0.37 Pa, and an isolated substrate bias of –60 V. The vacuum deposition chamber was baked with external sleeves for an hour before the deposition, in order to reduce the base pressure for each deposition (~10^{-4} Pa). The current density applied to the Bi target, J_{Bi}, was set to 0.19 $mA \cdot cm^{-2}$.

High-resolution transmission electron microscopy (HRTEM), high angle annular dark-field scanning transmission electron microscopy (HAADF-STEM), bright field scanning transmission electron microscopy (BF-STEM) and energy-dispersive X-ray spectroscopy (EDX) observations were carried on for ZnO:Ga,Bi thin film deposited on Si substrate, out at the International Iberian Nanotechnology Laboratory (INL), Braga, Portugal. For this, a FEI Model Titan ChemiSTEM 80-200 and a FEI Model Titan Themis 60-300 electron microscopes were used, both equipped with a field emission gun (X-FEG), Cs probe corrector, and super X EDX detectors, operating at 200 kV. Lamellae preparation was performed with a FEI Helios NanoLab 450S Focus Ion Beam equipment, operating with a Ga gun. Due to this type of gun, Ga could not be atomically quantified in the analysed films.

Temperature-dependent (18-300 K) X-ray absorption spectroscopy study of ZnO:Bi,Ga thin films was performed with the goal to determine the coordination environment of the dopant ions (Bi, Ga) and their influence on ZnO film structure. X-ray absorption experiments were done in transmission and fluorescence modes at P65 Applied XAFS beamline [18] of the HASYLAB/DESY PETRA III storage ring, operated at energy E=6.08 GeV and current I=95 mA in top-up 40 bunch mode. Commercial polycrystalline oxide powders (hex-ZnO, β-Ga_2O_3 and α-Bi_2O_3) were used for reference. Uncoated and Rh-coated silicon plane mirrors were employed for the harmonic rejection. A fixed-exit Si(111) and Si(311) monochromators were used for the K-Zn/Ga and L_3-Bi edges, respectively. X-ray absorption spectra were collected in transmission mode using two ionization chambers, whereas passivated implanted planar silicon (PIPS) detector was used in fluorescence mode. The Oxford Instruments liquid helium flow cryostat was used to maintain the required sample temperature in the range of 10-300 K. The reference samples for transmission measurements were prepared from powders, which were gently milled in an agate mortar and deposited on a Millipore membrane with a thickness to get the absorption edge jump $\Delta\mu \approx 1$. Thin-film samples deposited on Kapton were packed in stacks with the optimized number of layers and measured in transmission (Zn K-edge) and fluorescence (Ga K-edge and Bi L_3-edge) modes. At the Bi L_3-edge, a nickel-containing filter was used to reduce strong background fluorescence originating from zinc.

Experimental X-ray absorption spectra were analyzed using a conventional procedure [19]. Temperature-dependent extended X-ray absorption fine structures (EXAFS) $\chi(k)k^2$

were extracted and their Fourier transforms (FTs) were calculated using the 10% Gaussian window-function. The contributions from the first (or first and second for ZnO) coordination shell(s) were isolated by back-FT and analyzed within the single-scattering harmonic approximation using the conventional EXAFS equation [19]. The required backscattering amplitude and phase shift functions for Zn-O (Ga-O, Bi-O) and Zn-Zn (Ga-Zn) atom pairs were calculated using ab initio self-consistent real-space multiple-scattering FEFF8.50L code [20,21]. The scattering potential and partial phase shifts were calculated within the muffin-tin (MT) approximation [20,21] for the clusters constructed based on ZnO and α-Bi_2O_3 crystallographic structure with a radius of 8 Å, centred at the absorbing Zn (Ga, Bi) atom. The photoelectron inelastic losses were accounted for within the one-plasmon approximation using the complex exchange-correlation Hedin-Lundqvist potential [22]. The amplitude reduction factor S_0^2 is included in the scattering amplitude [20,21], calculated by the FEFF code, and no additional correction of the EXAFS amplitude was performed. The analysis yielded a set of structural parameters, such as coordination numbers (*N*), interatomic distances (*R*) and mean-square relative displacements (MSRDs) (σ^2), also known as the Debye-Waller factors.

A Bruker AXS D8 Discover system equipped with the copper anode X-ray tube (CuKα radiation) was used for X-ray diffraction experiments (XRD) in the grazing incidence geometry to probe the crystallinity, texture and phase composition of the films grown on Si substrates.

The X-ray photoelectron spectroscopy measurements were carried out for all films deposited on Si substrates using monochromatic Al-Kα radiation (1486.6 eV) from a Kratos Axis-Supra instrument, from 3Bs Group, University of Minho. Photoelectrons were collected from a take-off angle of 90º relative to the sample surface. The measurement was done in a Constant Analyser Energy mode (CAE) with a 160 eV pass energy and 15 mA of emission current for survey spectra and 40 eV pass energy for high-resolution spectra, using an emission current of 15 mA. Charge referencing was done by setting the lower binding energy of the C1s hydrocarbon peak at 284.8 eV; an electron flood gun was used to minimize surface charging.

μ-Raman spectra for all samples deposited on Si substrates were measured at RT using a Jobin-Yvon LabRaman HR spectrometer equipped with a grating of 600 grooves/mm and a multi-channel air-cooled (−70 ◦C) CCD detector, in the backscattering geometry, using the 442 (2.805 eV) and 325 nm (3.815 eV) excitation line of a He–Cd laser. The excitation laser was focused with a 50× objective (NA=0.5; WD= 10.6 mm) onto the sample surface. The spectra were acquired with an experimental error of ± 2 cm^{-1}.

3. Results and discussion

3.1 X-ray absorption experiments

3.1.1. Zn K-edge

The experimental Zn K-edge EXAFS $\chi(k)k^2$ spectra measured at 18 K are compared for all samples in Fig. 1. A particular focus is regarded on the analysis of the first two peaks in FTs. The detailed analysis of the full Zn K-edge EXAFS spectrum for the crystalline

hex-ZnO can be found in [23]. The first peak, at approximately 1.5 Å distance from the main Zn^{2+} cation, corresponds to the first coordination shell of zinc composed of oxygen atoms, whereas the second peak at about 3 Å corresponds mainly to the second coordination shell composed of zinc atoms. Note that the EXAFS spectra for all samples have similar overall shapes. However, when comparing to hex-ZnO reference powder, all ZnO-based thin films have slightly stronger disorder leading to the damping of the EXAFS oscillations at high *k*-values and to a reduction of the peak amplitudes in FTs, which is more noticeable for outer coordination shells of zinc located at distances above 2 Å. Additionally, the FTs for ZnO films doped with gallium have slightly different shapes of the first shell peak located at ~1.5 Å.

The contributions from the first two coordination shells around Zn atoms were isolated by Fourier filtering procedure in the *R*-range of 0.8-3.5 Å and fitted using the two-component model within the single-scattering harmonic approximation [19]. During the fit, the values of coordination numbers were fixed at the crystallographic ones for hex-ZnO [23], whereas the interatomic distances and the MSRDs were free parameters. The obtained MSRDs for Zn-O and Zn-Zn atom pairs in the first and second coordination shells of zinc, respectively, are shown in Fig. 2. The difference in the interatomic distances between various samples turned out to be small with the average values of *R*(Zn-O) = 1.97±0.02 Å and *R*(Zn-Zn) = 3.24±0.02 Å.

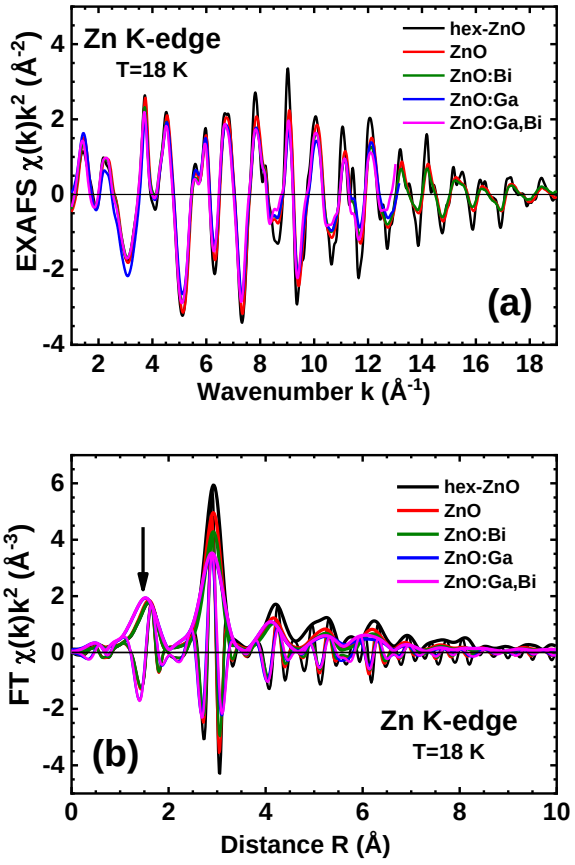

Fig. 1. (a) Zn K-edges EXAFS $\chi(k)k^2$ spectra and (b) respective Fourier transforms (FTs) for hex-ZnO powder and undoped (ZnO) and doped (ZnO:Bi, , ZnO:Ga, ZnO:Ga,Bi) thin films at 18 K.

As one can see in Fig. 2, the MSRDs for all samples have close temperature dependences, but those related to the thin films are larger than the MSRDs of polycrystalline hex-ZnO powder due to the presence of static disorder. For pure ZnO and ZnO:Bi thin films the static disorder is present in the coordination shells of zinc, starting from the second one. However, all coordination shells of zinc are affected by the static disorder in ZnO:Ga and ZnO:Ga,Bi films, where the largest difference in the second coordination shell reaches $\Delta\sigma^2 \approx 0.003\text{-}0.004$ Å^2, compared to the first shell $\Delta\sigma^2 \approx 0.001$ Å^2. Thus, according to the MSRD values, the thin films can be separated into two groups, with the largest MSRD values for the films doped with gallium. This means that gallium doping produces the strongest effect on the zinc oxide structure.

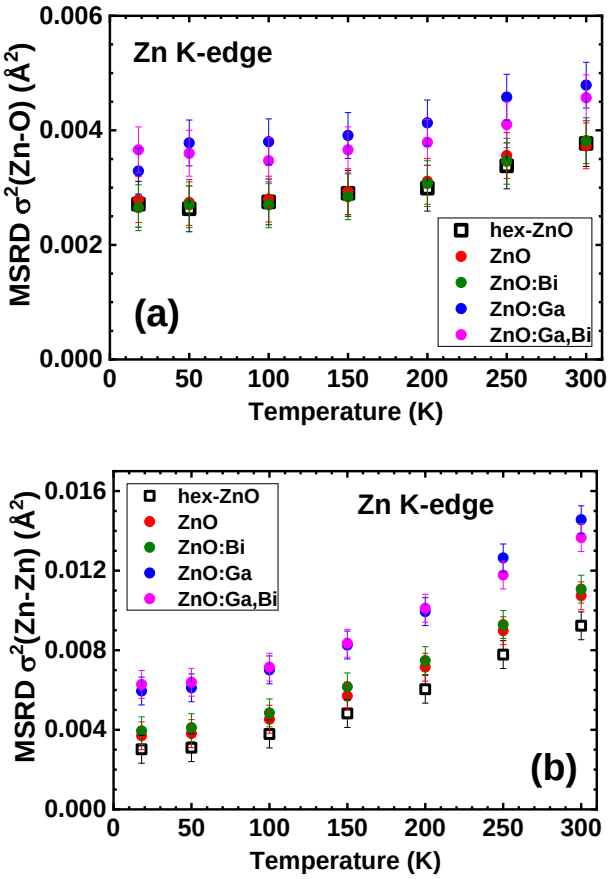

Fig. 2. Temperature-dependence of the mean-square relative displacements (MSRDs), for (a) Zn–O and (b) Zn–Zn atom pairs in the first and second coordination shells of zinc, respectively, for hex-ZnO powder, undoped (ZnO) and doped (ZnO:Bi, ZnO:Ga, ZnO:Ga,Bi) thin films.

3.1.2. Ga K-edge

The analysis of the Ga K-edge EXAFS in ZnO films is a challenging task due to a short distance (about 700 eV) between the Zn and Ga K-edges. As a result, the EXAFS

oscillations from the Zn K-edge interfere with those from the Ga K-edge (Fig. 3). The effect is especially pronounced at low temperatures (18 K), where thermal disorder is less strong, and the EXAFS oscillations have larger amplitude at high-*k* values. Upon increasing temperature, the thermal disorder becomes sufficiently large to significantly damp the Zn K-edge EXAFS oscillations before the Ga K-edge, thus allowing their separation and making the analysis more reliable. Therefore, only experimental data measured at 300 K were analyzed at the Ga K-edge.

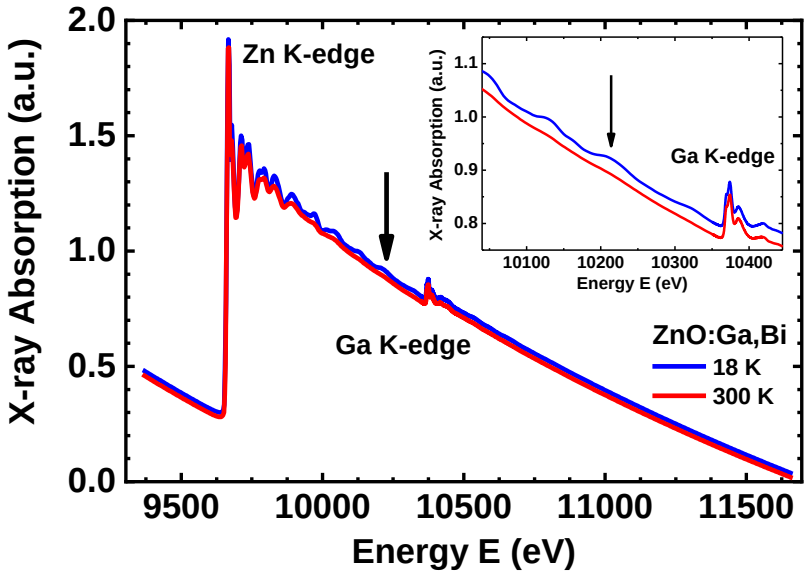

Fig. 3. Zn (9659 eV) and Ga (10367 eV) K-edges X-ray absorption spectra of ZnO:Ga,Bi thin film at 18 and 300 K. The insert shows an enlarged range close to the Ga K-edge. Arrow indicates a large amplitude of the EXAFS oscillations from the Zn K-edge at 18 K.

The normalized Ga and Zn K-edges XANES spectra for β-Ga_2O_3 powder and doped ZnO:Ga and ZnO:Ga,Bi thin films measured at 300 K are compared in Fig. 4. The similarity of the XANES spectra at two edges for the film suggests that gallium atoms substitute zinc. The main difference between Ga and Zn K-edge XANES spectra is attributed to the local structure relaxation occurring around gallium atoms. This conclusion is well supported by a comparison of the Ga and Zn K-edges EXAFS spectra (Fig. 5(a)), which are rather similar, taking into account the smaller signal-to-noise ratio of the Ga K-edge EXAFS measured in the fluorescence mode. Also, their FTs match at least up to 4.5 Å (Fig. 5(b)). Note that the Ga K-edge XANES and EXAFS spectra of ZnO:Ga and ZnO:Ga,Bi thin films are very close, which indicates the similarity of the gallium environment in the two films.

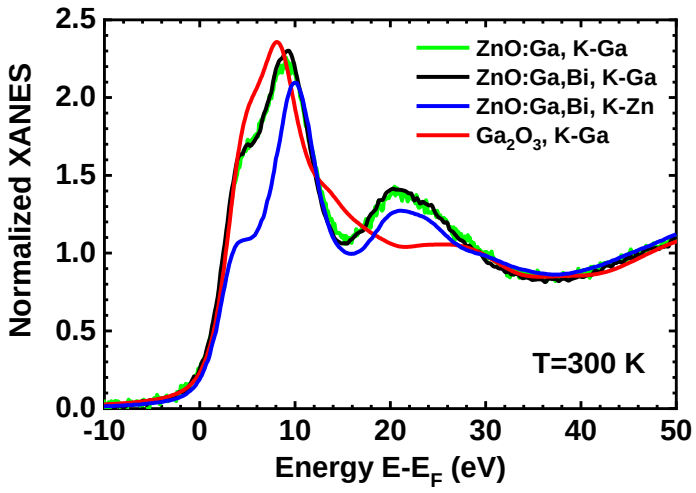

Fig. 4. Comparison of the normalized Ga and Zn K-edges XANES for β-Ga_2O_3 powder and doped ZnO:Ga and ZnO:Ga,Bi thin films at 300 K. Energy scale is relative to the Fermi level E_F.

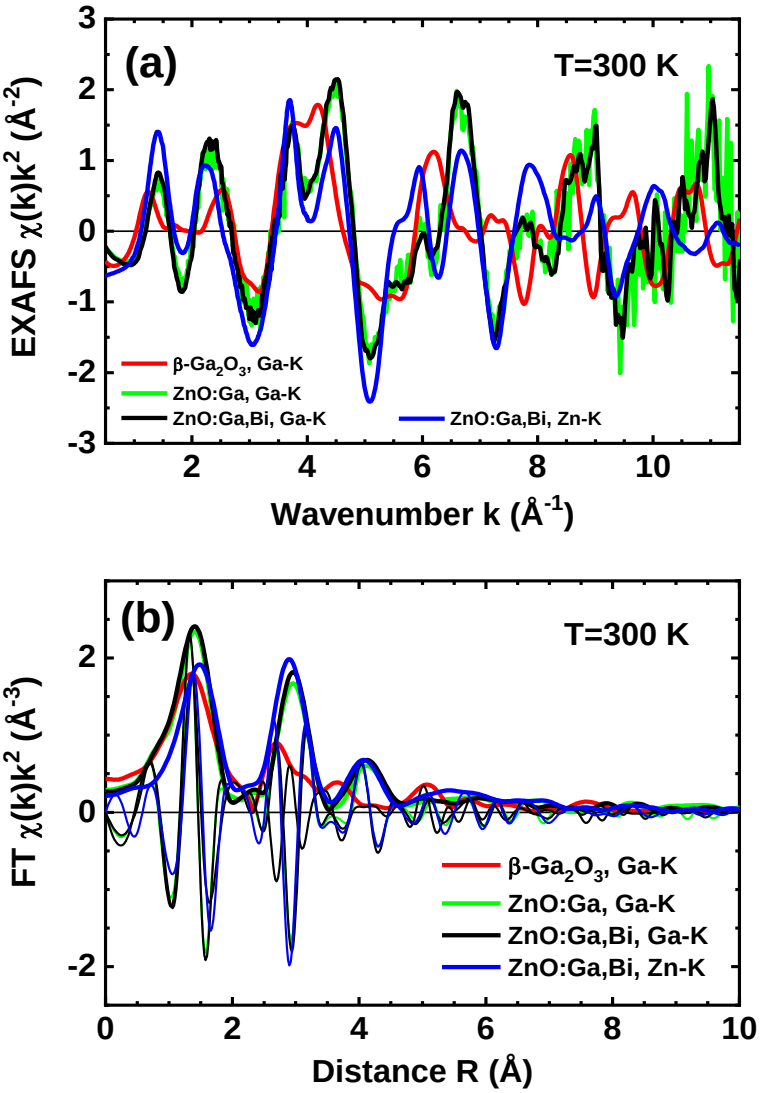

Fig. 5. (a) Ga and Zn K-edges EXAFS $\chi(k)k^2$ spectra and (b) their Fourier transforms (FTs) for β-Ga_2O_3 powder and doped ZnO:Ga and ZnO:Ga,Bi thin films at 300 K.

The best-fit analysis of the Ga K-edge EXAFS contributions from the first two coordination shells of gallium in ZnO:Ga and ZnO:Ga,Bi thin films were performed within the single-scattering harmonic approximation [19]. The values of the obtained structural parameters in both films coincide within the error of fitting. The interatomic distances are *R*(Ga-O) = 1.87±0.03 Å and *R*(Ga-Zn) = 3.26±0.02 Å. The distance *R*(Ga-O) is typical for tetrahedrally coordinated gallium atoms [24] and is shorter by about 0.1 Å than *R*(Zn-O) = 1.97 Å, suggesting that some relaxation of the local environment occurs in the films around the substituting gallium atoms due to their smaller ionic radius. In tetrahedral coordination, Zn^{2+} has an ionic radius of 0.60 Å, whereas the ionic radius of Ga^{3+} is 0.47 Å [25]. At the same time, the distances *R*(Ga-Zn) and *R*(Zn-Zn) in the second coordination shell are close within the error bars. The MSRD value for the Ga-O bonds is equal to σ^2(Ga-O) ≈ 0.0026±0.0004 Å^2. This value is slightly smaller than that for the Zn-O bonds σ^2(Zn-O) ≈ 0.0038±0.0004 Å^2 in polycrystalline hex-ZnO, indicating stronger Ga-O bonding.

Thus, one can conclude that the doping of ZnO with gallium results in additional structural disorder caused by the relaxation of the local environment around gallium ions, which have a smaller size than zinc ions.

3.1.3. Bi L_3-edge

The study of ZnO thin films weakly doped with bismuth at the Bi L_3-edge (13419 eV) is a complex task in fluorescence mode due to the strong background coming from the zinc fluorescence. This phenomenon was partially attenuated in the present study by using nickel-containing filter. However, the quality of the experimental data is worse at the Bi L_3-edge than at the Ga K-edge. The Bi L_3-edge XANES spectra of α-Bi_2O_3 powder and ZnO:Ga,Bi thin film are compared in Fig. 6. The positions of the shoulder A and the main edge B coincide well in both compounds, suggesting 3+ oxidation state for bismuth ions in the film.

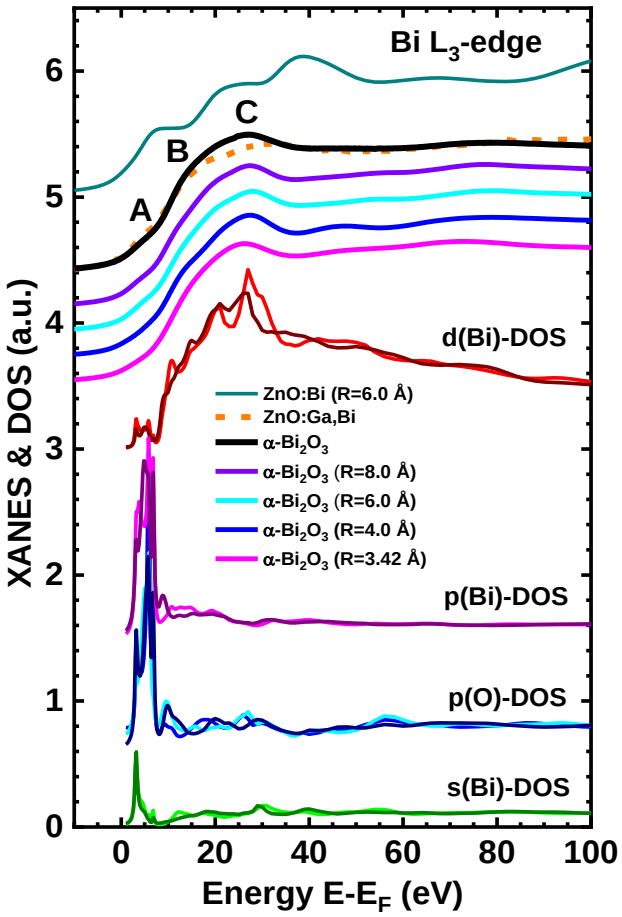

Fig. 6. Comparison of the experimental Bi L_3-edge XANES spectra for α-Bi_2O_3 powder (black solid curve) and ZnO:Ga,Bi thin film (dashed orange curve) at 300 K with the results of ab initio XANES calculations by the FDMNES code. Theoretical models include Bi-doped ZnO with the cluster radius R=6.0 Å (upper curve) and α-Bi_2O_3 with the cluster radii R=3.42, 4.0, 6.0 and 8.0 Å. Selected partial densities of states (DOS) are also shown for non-equivalent Bi and O atoms in α-Bi_2O_3. The energy scale is relative to the Fermi level E_F.

To understand the origin of all features in the Bi L_3-edge XANES, the ab initio real-space FDMNES code [26,27] implementing the finite difference method (FDM) was used. The relativistic FDM calculations were performed with self-consistent potential within the dipole approximation using the energy-dependent real Hedin-Lundqvist exchange-correlation potential [26,27]. Calculated XANES spectra were broadened to account for the core-hole level widths (Γ(L_3-Bi) =5.6 eV [28]) and other multielectronic phenomena. The energy origin was set at the Fermi level E_F. The clusters of different size (radius) were constructed from the crystallographic α-Bi_2O_3 structure [29], centred at the absorbing Bi atom. Besides this, the structural model based on the hex-ZnO structure with Bi atom substituting Zn was also evaluated.

The calculated Bi L_3-edge XANES spectra are compared with the experimental ones in Fig. 6. Selected partial densities of states (DOS) for s(Bi), p(Bi), d(Bi) and p(O) contributions in α-Bi_2O_3 are also shown. They were evaluated for all non-equivalent Bi and O atoms in α-Bi_2O_3 structure [29]. Note that the smallest α-Bi_2O_3 cluster with a radius of 3.42 Å includes only oxygen atoms in the first coordination shell of bismuth. The α-

Bi_2O_3 cluster with a radius of 6 Å including 57 atoms is large enough to reproduce all experimentally observed features. At the same time, the substitutional model based on the hex-ZnO structure (upper curve in Fig. 6) deviates strongly from the experimental data, suggesting that Bi ions do not enter the ZnO wurtzite cell.

Bismuth ion has a ground-state electron configuration of $[Xe]4f^{14}5d^{10}6s^26p^3$ and, depending on the oxidation state, the valence electrons are situated either at the 6s or 6p orbitals. The Bi L_3-edge XANES allows one to probe the s and d empty electron states, however, the large value of the core-hole level width Γ at the Bi L_3-edge results in a strong broadening of XANES. Better experimental resolution can be obtained using high energy resolution X-ray absorption spectroscopy, which was employed recently to study several bismuth compounds including α-Bi_2O_3 [30]. The Bi L_3-edge XANES of ZnO:Ga,Bi thin film has no pre-edge peak due to the $2p \rightarrow 6s$ transition, which was observed in $NaBiO_3$ in [30], meaning 6s(Bi) states are occupied, and, thus, bismuth ions have oxidation state 3+ in the film. Therefore, similar to Bi_2O_3 [30], the Bi L_3-edge XANES in ZnO:Ga,Bi thin film is due to $2p_{3/2} \rightarrow ns$ ($n \geq 7$) and $2p_{3/2} \rightarrow nd$ ($n \geq 6$) transitions, with the d(Bi)-states producing major contribution and the s(Bi)-states giving minor contribution. The shoulder A has also a strong admixture of the O and Bi p-states. The Bi d-states dominate at the main edge B and above it (peak C). Note that the peak C is split into two components in high energy resolution XANES measured in [31]. This splitting of the d(Bi)-DOS (the peaks at 20 and 27 eV above the Fermi level E_F in Fig. 6) is well reproduced in our calculations.

The Bi L_3-edge EXAFS spectra of α-Bi_2O_3 powder and ZnO:Ga,Bi thin film are reported in Fig. 7. The EXAFS oscillations from both samples have some similarities. However, they have slightly different main frequency and deviate also in high-frequency contributions. The FTs for both samples are dominated by the peak at 1.6 Å, while a few small peaks above 2.4 Å are also visible. These FTs differ significantly from those at the Zn and Ga K-edges in Figs. 1(b) and 5(b): the first peak is located at a longer distance, whereas the next peaks are at much lower distances, indicating that Bi ions are located in an environment that is different from that of Zn and Ga ions.

The first peak contribution was isolated by the Fourier filtering procedure in the *R*-space range of 0.9-2.2 Å and analyzed within the single-scattering harmonic approximation [19]. Note that, due to the strongly distorted local environment of Bi in α-Bi_2O_3 [29], this *R*-range includes mainly the contribution from the nearest 3 oxygen atoms located between 2.1 and 2.3 Å. The obtained value of the average Bi-O distance in the film *R*(Bi-O) = 2.11±0.02 Å is slightly shorter than in α-Bi_2O_3 *R*(Bi-O) = 2.19±0.02 Å, in agreement with the difference in the frequency of the first shell EXAFS spectra shown in Fig. 7(a). The MSRDs σ^2(Bi-O) is equal to 0.006±0.001 $Å^2$ for both α-Bi_2O_3 and ZnO:Ga,Bi thin film. The larger value of the MSRDs for Bi-O bonds than for Zn-O and Ga-O bonds can be attributed to a spread of the Bi-O bond lengths.

Thus, it is concluded that Bi^{3+} ions do not substitute zinc and are likely located at the ZnO grain boundaries. Such conclusion agrees also with the fact that the ionic radius of Bi^{3+} is about 1.03 Å, being nearly twice larger than that of Zn^{2+} (0.60 Å) [25], making the incorporation of Bi^{3+} ions into ZnO film difficult [31,32]. Segregation of bismuth oxide

at ZnO grain boundaries has also been observed by scanning electron microscopy and energy-dispersive X-ray analysis in [33].

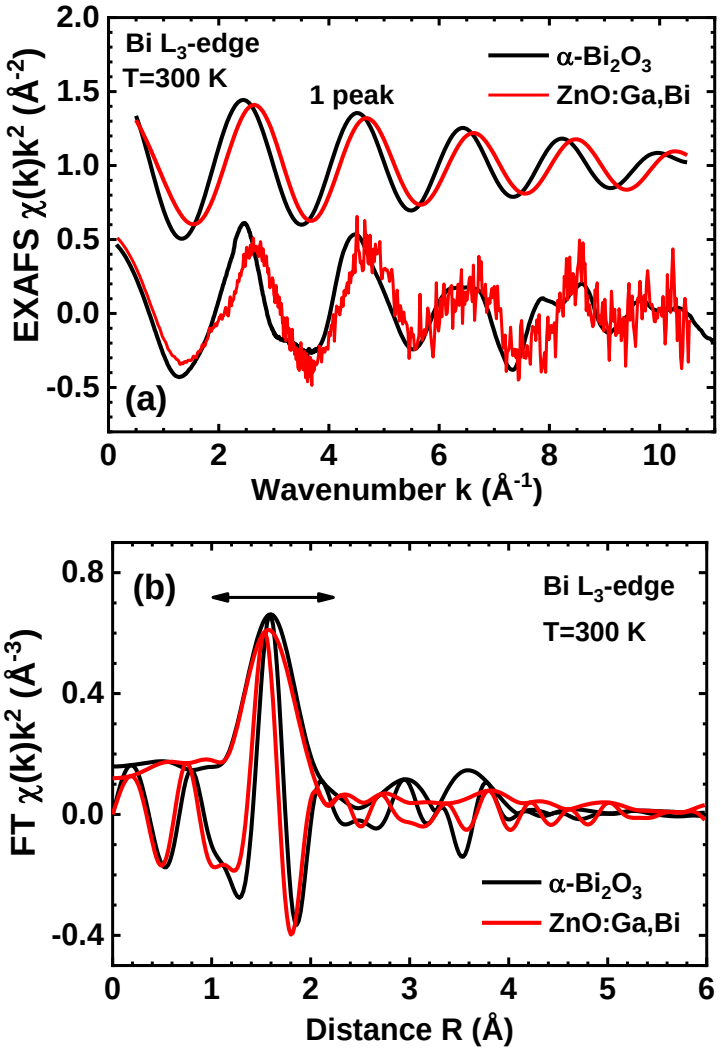

Fig. 7. (a) Bi L_3-edge EXAFS $\chi(k)k^2$ spectra and (b) their Fourier transforms (FTs) for α-Bi_2O_3 powder and doped ZnO:Ga,Bi thin film at 300 K. The EXAFS contribution from the first peak, indicated in (b), is also shown in (a).

3.2 X-ray diffraction

Fig. 8 shows the grazing incidence X-ray diffraction (GIXRD) patterns of undoped ZnO, ZnO:Bi; ZnO:Ga and ZnO:Ga:Bi thin films, for $20^o < 2\theta < 60^o$, with an incidence angle of 1.5 °. For undoped ZnO and ZnO:Ga, all diffraction peaks were assigned to a ZnO phase with the hexagonal wurtzite crystal structure, P63mc (186). The vertical dot lines indicate the peak position from this phase (ICDD card 01-089-0510). Under the resolution of GIXRD, no other phases were detected. The introduction of Ga onto the film decreases the relative diffraction peak intensity of (002) planes compared to the (100) and (101) planes, as already observed by J. Hu and R. Gordon [34]. However, Bi doping produces a larger effect.

F. C. Correia, J. M. Ribeiro, A. Kuzmin, I. Pudza, A. Kalinko, E. Welter, A. Mendes, J. Rodrigues, N. Ben Sedrine, T. Monteiro, M. R. Correia, C. J. Tavares, The role of Ga and Bi doping on the local structure of transparent zinc oxide thin films, J. Alloys Compd. 870 (2021) 159489. Doi: 10.1016/j.jallcom.2021.159489.

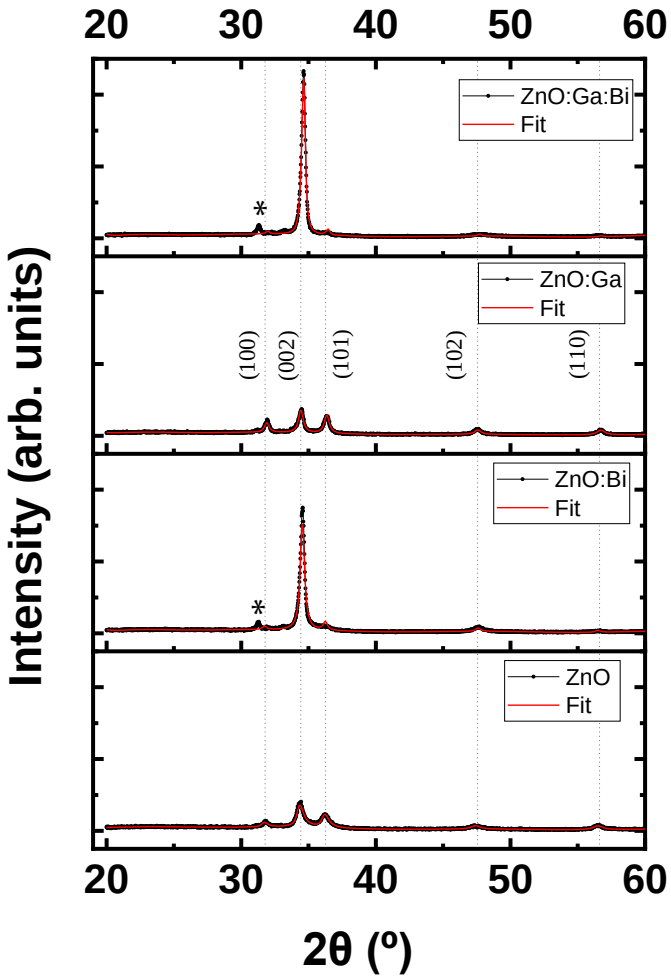

Fig. 8 - GIXRD patterns for ZnO, ZnO:Bi, ZnO:Ga and ZnO:Ga:Bi thin films. The same vertical scale is used for all patterns.

ZnO:Bi and ZnO:Ga:Bi films present a different behaviour. Firstly, the intensity of the main peak at 34.43º, corresponding to the (002) reflection, is more than five times larger than in the case of ZnO and ZnO:Ga thin films. This enhancement in texture was already reported by Krongarrom et al. [35]. In symmetric θ-2θ X-ray diffraction, the observed reflections are associated with lattice planes parallel to the film surface, and the preferential growth direction can be correlated with surface energy, which is lowest for (002) hexagonal crystal planes [35]. However, GIXRD probes randomly orientated crystals in the film bulk. Hence, it can be inferred that, as well as having a preferred orientation, the grains are elongated along [001] direction. A possible explanation for this can be related to evidence of Bi segregation at grain boundaries, as observed by Jood et al. [32]. On the other hand, other authors have reported on the effect of edge dislocations distributed in specific interfacial crystal planes between Bi segregation at grain boundaries and specific crystal planes of SnTe phases [36,37]. An unassigned peak (marked with an asterisk in Fig. 8) is present at 31.2±0.4º for the Bi-doped films. None of the known Zn, ZnO, Ga_2O_3, $ZnGa_2O_4$, Bi, Bi_2O_3 or Bi_2O phases reported in the

literature phase include a reflection at that position. These phases were tentatively included in the Rietveld fits although lacking structural match. Table 1 includes the lattice parameters (*a*, *c*), crystallite size (*g*) and nearest neighbour Zn–O bond distance (b_1) derived from the Rietveld fits to the XRD patterns for undoped ZnO, ZnO:Bi, ZnO:Ga and ZnO:Ga:Bi films. The bond distance was estimated from:

$$u = \left(\frac{1}{3}\right)\left(\frac{a^2}{c^2}\right) + \frac{1}{4} \qquad \text{Equation 1}$$

$$b_l = \sqrt{\frac{1}{3}a^2 + c^2\left(\frac{1}{2} - u\right)^2} \qquad \text{Equation 2}$$

From these parameters, it is not possible to conclude if Ga or Bi is introduced in the ZnO structure, since the bond length variation is within the experimental error (1.98±0.20 Å to 1.99±0.20 Å), albeit close to the obtained value of 1.97 Å from the EXAFS results obtained for the Zn K-edge in section 3.1. The grain size varies between 30 - 44 for all films, being the largest for ZnO:Ga:Bi.

Table 1 - Lattice parameters (*a*, *c*), crystallite size (*g*) and nearest neighbour Zn–O bond distance (b_1) derived from the Rietveld fits of the XRD patterns for undoped ZnO, ZnO:Bi, ZnO:Ga and ZnO:Ga:Bi films.

Film	*a* (Å)	*c* (Å)	*g* (nm)	b_1 (Å)
ZnO	3.26 ±0.10	5.23 ±0.10	41	1.98 ±0.20
ZnO:Bi	3.26 ±0.10	5.22 ±0.10	32	1.98 ±0.20
ZnO:Ga	3.26 ±0.10	5.24 ±0.10	30	1.99 ±0.20
ZnO:Ga:Bi	3.26 ±0.10	5.22 ±0.10	44	1.98 ±0.20

3.3 Electron Microscopy

In the HAADF-STEM micrograph seen in Fig. 9, the ZnO:Ga,Bi thin film is viewed down the [001] zone of the wurzite crystal structure of ZnO. From the fast Fourier transforms (FFTs) in three different grains, the ZnO wurtzite structure is established, as confirmed from the XRD experiments in section 3.2. Bismuth is clearly seen in the grain boundaries, and is far brighter than the zinc oxide, as expected for its higher atomic number (Z) contrast.

F. C. Correia, J. M. Ribeiro, A. Kuzmin, I. Pudza, A. Kalinko, E. Welter, A. Mendes, J. Rodrigues, N. Ben Sedrine, T. Monteiro, M. R. Correia, C. J. Tavares, The role of Ga and Bi doping on the local structure of transparent zinc oxide thin films, J. Alloys Compd. 870 (2021) 159489.
Doi: 10.1016/j.jallcom.2021.159489.

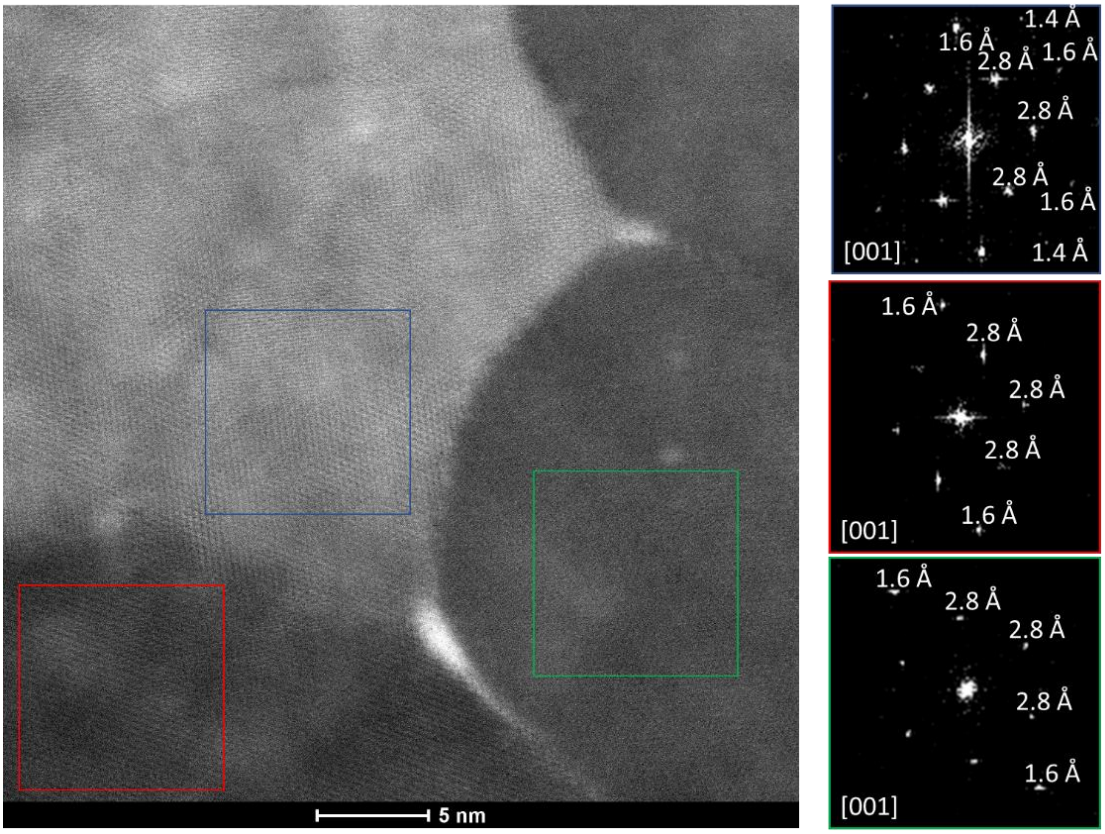

Fig. 9 - HAADF-STEM and FFTs for the ZnO:Ga,Bi thin film along [001], with each of the three FFTs in a coloured box coming from the corresponding box on the main micrograph. Bi atoms are located at the grain boundaries (higher contrast) that delimit ZnO:Ga grains.

From the EDX maps in Fig. 10, it is possible to discern the locations of Zn and Bi atoms in a zone of the ZnO:Ga,Bi film. Bi atoms are clearly situated at the ZnO grain boundaries. A magnification of one of these grain boundaries is observed in the HAADF-STEM micrograph in Fig. 11. From the FFTs of the TEM micrographs and direct measurement of the lattice spacings, it can be inferred that the diffraction arises from crystals with 2.8 Å and 3.2 Å plane spacing, either from α-Bi_2O_3 (monoclinic, P-21/c) or β-Bi_2O_3 (tetragonal, P-421c). The observed crystals in the grain boundary are not fully crystalline, and thus it leads to difficulty in analysing the crystal structure, also due to its size. Upon analysing with detail these grains, and others (not shown) in the lamellae, there is a good chance that in some of the observed grain boundaries, ZnO is forcing Bi_2O_3 into a matching (templating) crystal structure.

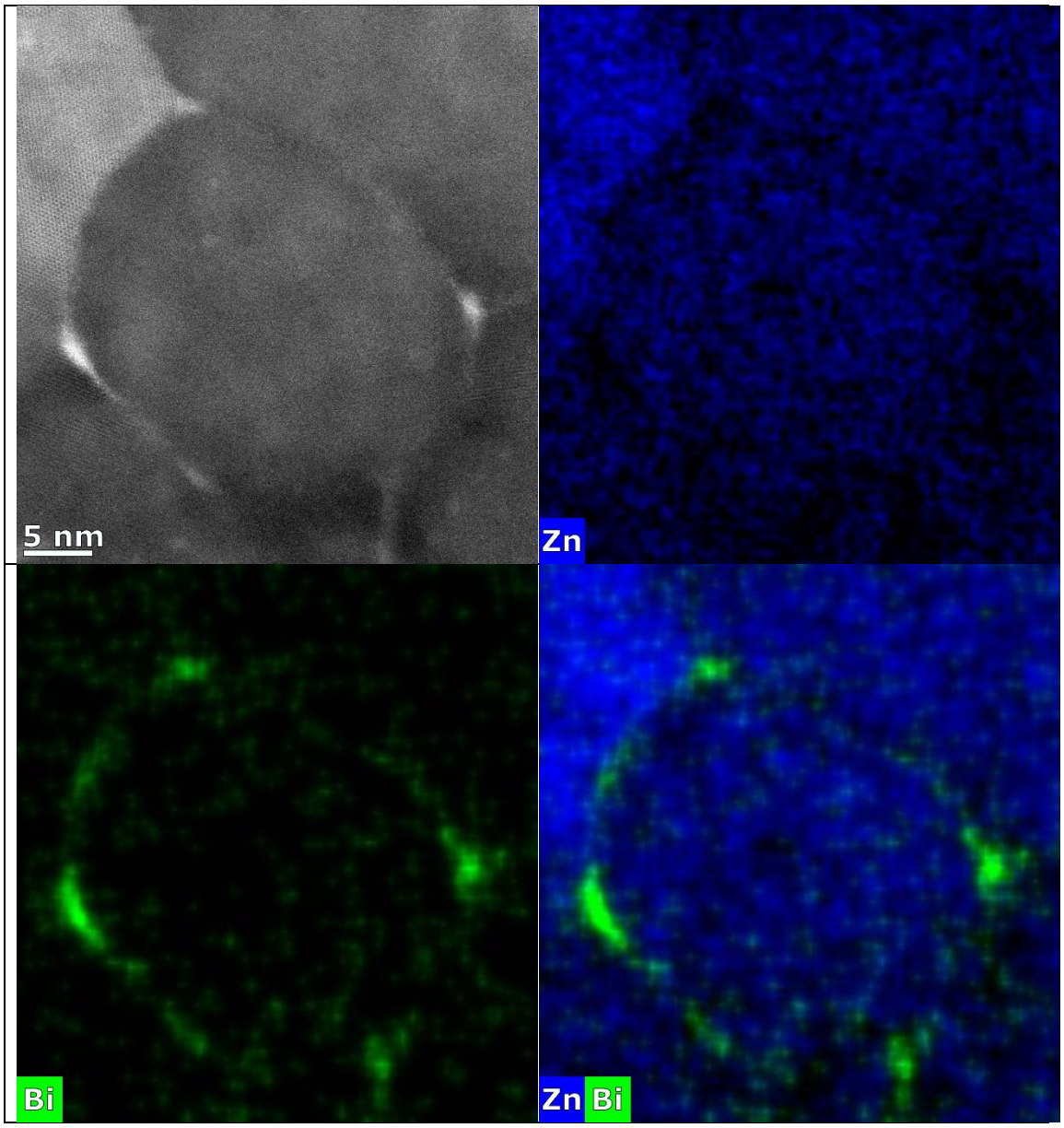

Fig. 10 – (clockwise from top) HAADF-STEM along [001] and respective Zn and Bi EDX maps for a ZnO:Ga grain of the ZnO:Ga,Bi thin film.

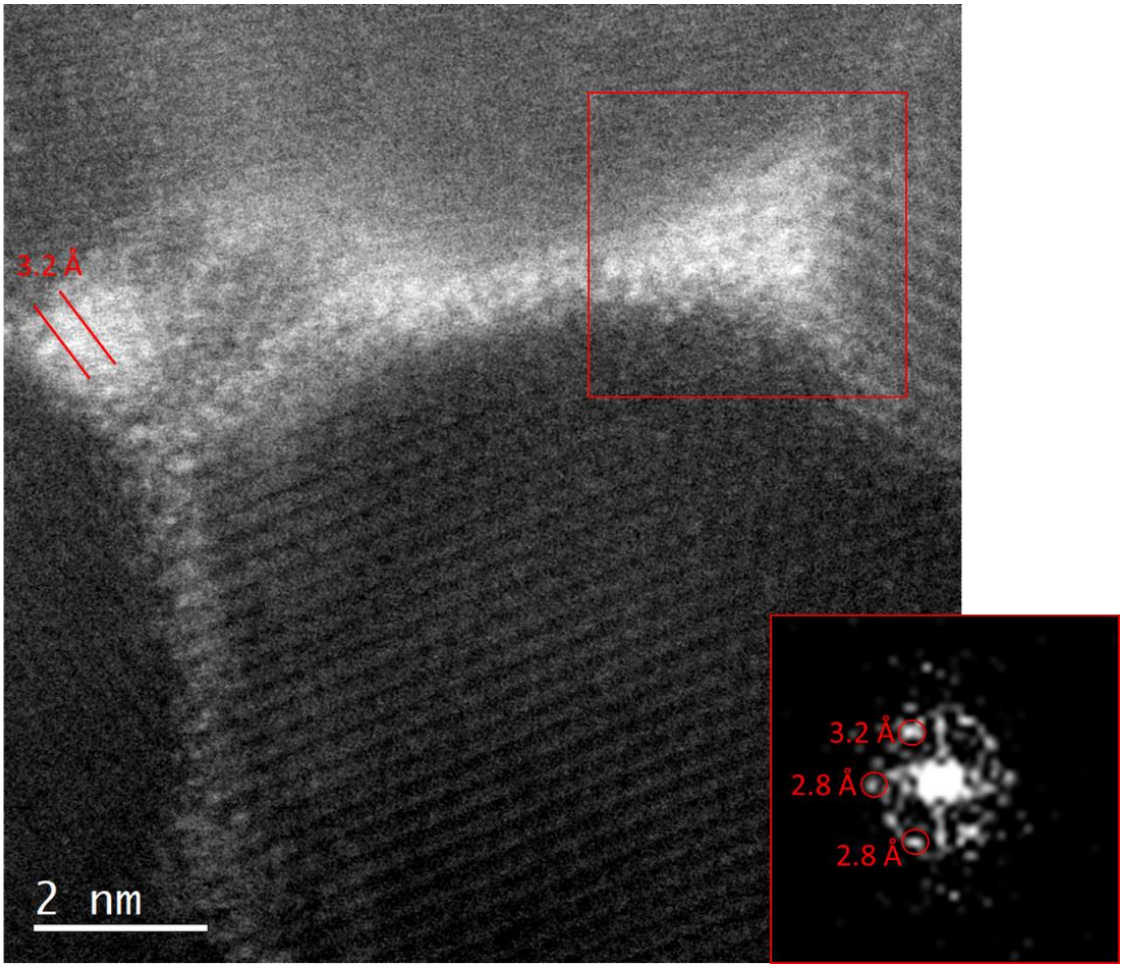

Fig. 11 – HAADF-STEM along [001] and an inset of the FFT of the area in the red box on the image, showing the crystal spacings of the Bi oxide in the grain boundary delimiting ZnO:Ga grains of a ZnO:Ga:Bi thin film, also seen in the other particle by direct measurements.

3.4 X-ray photoelectron spectroscopy

The XPS spectra and respective fits to main photoelectron lines (Zn 2p, O 1S, Ga 2p and Bi 4f) for a ZnO:Ga,Bi thin film are presented in Fig. 12. The Zn $2p_{3/2}$ core line was fitted with one component (1021.5 eV; FWHM=1.8 eV), which is ascribed to Zn-O bonds [38] is shown in Fig. 12(a). The spin-orbit energy separation of $2p_{3/2}$-$2p_{1/2}$ is 23.1 eV, with a peak area ratio $A2p_{3/2}/A2p_{1/2}$ = 0.5. It can be found in the literature that the binding energy ascribed to the Zn $2p_{3/2}$ core line lies in the ranges of 1021.7 - 1022.0 eV and 1021.4 - 1021.7 eV for bulk ZnO and Zn metal, respectively [39,40]. The reduction in binding energy can be associated with Ga^{3+} substitution in the ZnO cell, as confirmed in a previous study for ZnO:Ga thin films [41]. The parameters from this XPS refinement (Unifit Scientific Software GmbH, Germany) are reported in Tables 2 and 3.

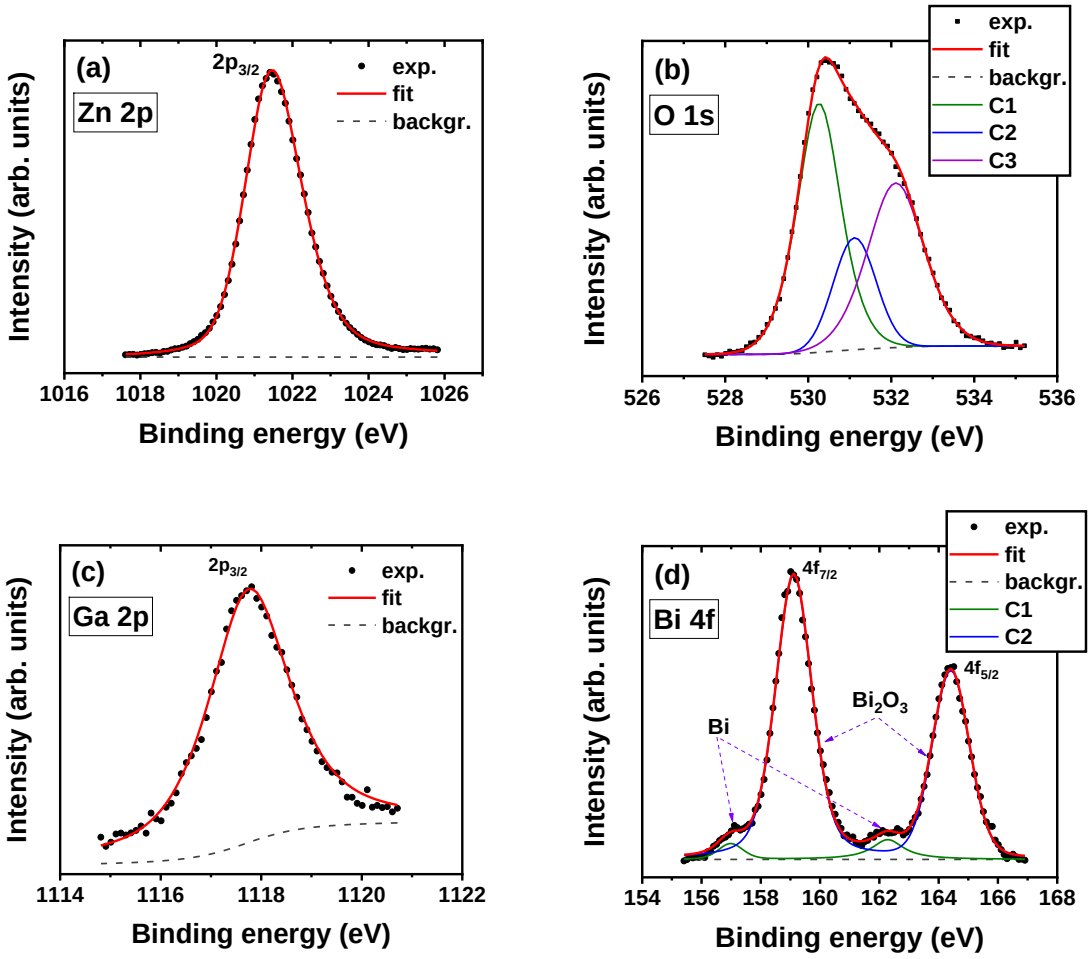

Fig. 12 – XPS spectra and respective fits to main photoelectron lines (Zn 2p, O 1S, Ga 2p and Bi 4f) for a ZnO:Ga,Bi thin film.

The O 1s core line in Fig. 12(b), for the ZnO:Ga,Bi thin film, was fitted with three components (C1, C2 and C3): the main component at 530.3 eV (C1) is credited to Zn-O bonds (FWHM of 1.3 eV); the second component (C2) centred at 531.3 eV (FWHM of 1.1 eV) is ascribed with defective oxygen (vacancies) and with Bi-O bonds; and at higher binding energies, 532.4 eV (FWHM of 1.2 eV), C3, corresponds to surface-adsorbed oxygen and hydroxides impurities [40,42]. The relative areas of C1 and C2 contributions are 60% and 40%, respectively, when disregarding surface impurities (C3). Component C2 of the O 1s photoelectron line, related to oxygen vacancies, discloses the prominence of the defective oxygen sites in the improvement of the electrical conductivity. The Ga $2p_{3/2}$ core line, in Fig. 12(c), was fitted with one contribution (1117.8 eV; FWHM= 1.9 eV) related to the Ga-O bonds in the ZnO matrix. No evidence of gallium oxide phases were discerned in the Ga-doped ZnO films. Finally, the Bi 4f core level, shown in Fig. 12(d), was fitted into peak doublets with a spin-orbit energy separation of $4f_{5/2}$-$4f_{7/2}$ = 5.3 eV and a peak area ratio $A_{4f5/2}/A_{4f7/2}$ = 0.75. Two contributions were fitted, with Bi $4f_{7/2}$ binding energies of 156.9 (FWHM= 1.2 eV) and 159.1 eV (FWHM= 1.1 eV), which

correspond to the metallic bismuth (8%) and oxidation state of Bi^{3+} in Bi_2O_3 (92%), respectively. From the quantification of these findings, it was possible to reach a composition close to the surface of 50.1 at.% for Zn, 46.1 at.% for O, 2.2 at.% for Ga and 1.6 at.% for Bi, for the ZnO:Ga,Bi thin film. Similarly, XPS refinements were produced for the undoped ZnO, ZnO:Ga and ZnO:Bi thin films, being the composition and other refinement parameters listed in Tables 2 and 3.

From the observation of Tables 2 and 3 it can be concluded that the undoped ZnO thin film is slightly sub stoichiometric in zinc (49.1 at.%), in respect to oxygen (50.9 at.%). This Zn deficiency is more prominent in the ZnO:Bi film, where the concentrations of Zn and O are 44.6 at.% and 53.4 at.%, respectively. The excess of oxygen is related to the existence of Bi_2O_3 at the grain boundaries, as seen from the STEM micrographs. The resulting Bi content is 2.0 at.%. Contrariwise, for the ZnO:Ga film, oxygen is deficient (46.9 at.%) in comparison to zinc (51.6 at.%). In this film, the combination of efficient Ga doping (1.5 at.%) and the enhancement of the O 1s C2 XPS peak ascribed to oxygen deficiency and vacancies, leads to the enhancement of the charge carrier concentration from ~10^{16} cm^3 (undoped ZnO) to ~10^{21} cm^3 (ZnO:Ga), and concomitantly the electrical conductivity, as reported elsewhere by the authors [43,44]. In fact, in Table 3, C2 component is highest (40%) for ZnO:Ga, when comparing to undoped ZnO (26%) and ZnO:Bi (30%), albeit being the same for the ZnO:Ga,Bi film. The Bi content in both ZnO:Bi and ZnO:Ga,Bi lies in the range of 1.6 – 2.0 at.%, being slightly highest for the former. As for the relative amount of Bi-metal bonds and Bi-O bonds, according to Table 3 for ZnO:Bi and ZnO:Ga,Bi, the latter has a higher level of Bi-O bonds (92%) and lower amount of Bi-metal bonds (8%), when comparing to ZnO:Bi (85% and 15% respectively). The Zn 2p and Bi 4f doublet separation is constant in all films, 23.1 eV and 5.3 eV, respectively.

Table 2 – Atomic quantification derived from the XPS fits.

Film	Composition (at.%)			
	Zn	O	Ga	Bi
ZnO	49.1	50.9	-	-
ZnO:Bi	44.6	53.4	-	2.0
ZnO:Ga	51.6	46.9	1.5	-
ZnO:Ga:Bi	50.1	46.1	2.2	1.6

Table 3 – Fitting parameters derived from the XPS peak refinements. C1 and C2 are the lower binding energies components in the O 1s core level spectra (Fig. 12b); Bi-Bi refers to metallic bismuth peaks, Bi-O to bismuth oxide peaks, in the Bi 4f core level (Fig. 12d).

Film	Binding energy (FWHM) (eV)				Relative areas (%)	
	Zn	C1 / C2	Ga	Bi-Bi / Bi-O	C1 / C2	Bi-Bi / Bi-O
ZnO	1021.6 (1.8)	530.0 (1.2) / 531.0 (1.3)	-	-	74 / 26	-
ZnO:Bi	1021.8 (1.7)	530.4 (1.3) / 530.9 (1.1)	-	157.2 (1.3) / 159.1 (1.0)	70 / 30	15 / 85
ZnO:Ga	1021.7 (1.9)	530.4 (1.4) / 531.4 (1.0)	1117.9 (1.7)	-	60 / 40	-
ZnO:Ga:Bi	1021.5 (1.8)	530.3 (1.3) / 531.3 (1.1)	1117.8 (1.9)	156.9 (1.2) / 159.1 (1.1)	60 / 40	8 / 92

3.5 μ-Raman spectroscopy

μ-Raman scattering (non-resonant and resonant) proven to be an important tool to assess information about structural properties of ZnO thin films and nanostructures [45–48], carrier concentration [49], microscopic environment of doping species in ZnO lattice, [50–53], as well as to analyse more specific aspects of lattice dynamics, such as isotopic effects[54] and phonon lifetimes [55], among others. Direct connections between the chemical environment of constituent atoms, the phonon-phonon and phonon-electron scattering properties of materials are valuable knowledge that can guide the search for disruptive solutions with the desired thermal transport and thermoelectric properties.

Figure 13(a) compares the Raman spectra measured upon excitation above (325 nm= 3.8 eV) and below (442 nm =2.8 eV) the ZnO, ZnO:Ga, ZnO:Bi, and ZnO:Ga,Bi films band gap at room temperature. For the (undoped) ZnO film, when exciting with 442 nm, three modes located in the vicinity of 439 cm^{-1}, 580 cm^{-1} and 1158 cm^{-1} are observed in the Raman spectrum. The mode at 439 cm^{-1} is assigned to the E_2 (high) phonon frequency [56] and is allowed by symmetry selection rules of wurtzite structure crystals in backscattering geometry [57]. The mode measured at 580 cm^{-1} is in between the A_1(LO) (574 cm^{-1}) and the E_1 (LO) (584 - 591 cm^{-1}) modes [46,55,58]. This registered intermediate-valued frequency can be analyzed in terms of its quasi-nature considering the polycrystalline nature of the ZnO films, as confirmed by the X-ray diffraction measurements (see Fig. 8). Raman scattering from crystal or nanocrystal axes that are not

the crystal-symmetry axes (i.e., not the *a* or *c* axes) result in what is known as quasi-modes, according to Loudon's model [59]. For small, but finite, phonon wavevector, those modes comprise mixed symmetry modes due to phonons propagating between the *a* and the *c* axes. The angular dispersion of the LO quasi-mode in the wurtzite structure predicted by Loudon's model is given by:

$$\omega^2(LO) = \omega^2_{A_{1(LO)}} cos^2(\theta) + \omega^2_{E_{1(LO)}} sin(\theta) \qquad \text{Equation 3}$$

where θ is the angle measured between the wave vectors of created phonons and the *c*-axis of the wurtzite structure that are in the laser spot probed size. Thus, the frequency of the LO mode measured with the 442 nm laser line should be representative of the LO frequencies possible over the crystallites having the orientation determined by the angle θ and probed within the laser spot size.

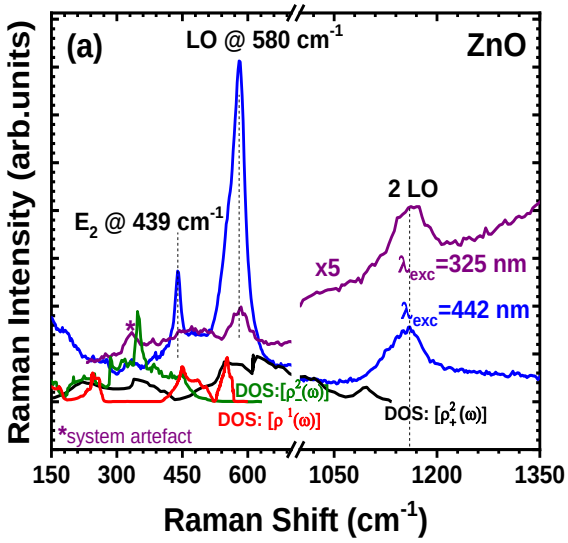

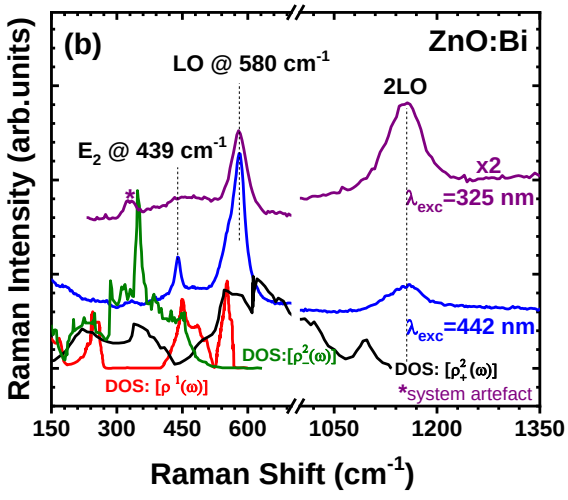

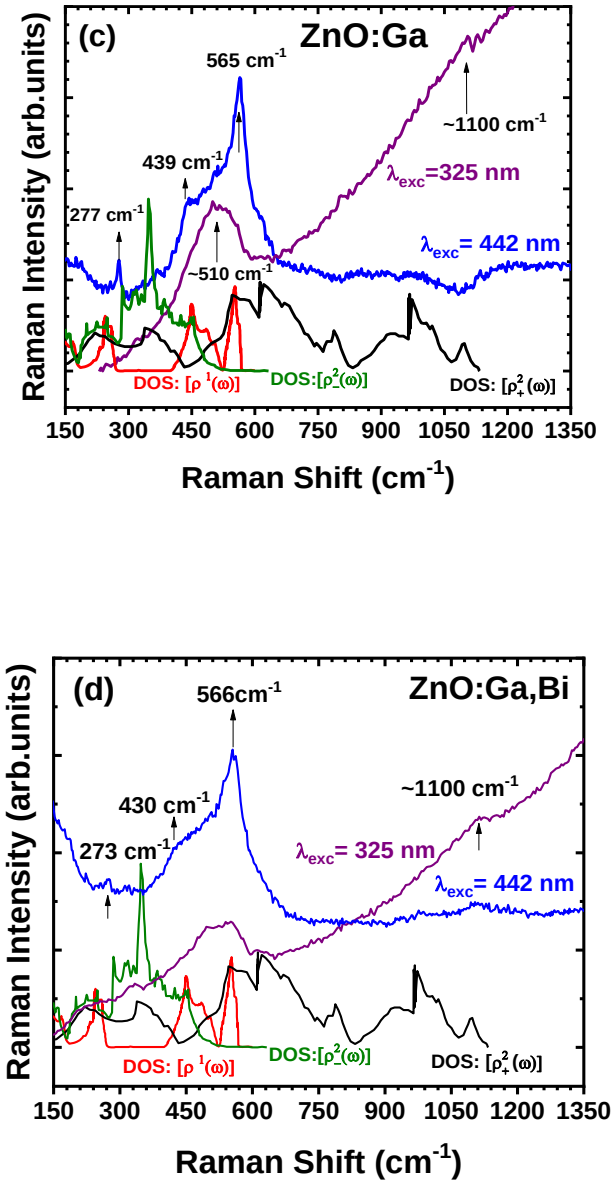

Fig. 13 - Comparison of RT μ-Raman spectra measured using the He:Cd laser line excitation of 442 nm (blue) and 325 nm (purple) for (a) undoped ZnO, (b) ZnO:Bi, (c) ZnO:Ga, and (d) ZnO:Ga,Bi thin films. The $[\rho^1(\omega)]$ one- phonon DOS (red), $[\rho^2_+(\omega)]$ two-phonon sum DOS (black), $[\rho^2_-(\omega)]$ two-phonon subtract DOS (green) from Serrano et al. [60] are include for comparison purposes.

In order to distinguish between Raman bands related to the wurtzite ZnO network and local vibrations (impurity modes) associated with the doping atoms it is essential to compare the Raman experimental spectra with the phonon density of states (DOS). The DOS reflects the influence of Raman disorder-activated phonons from the entire Brillouin zone centre and the second order process, as well as the influence of the nanocrystalline nature of the undoped ZnO film on momentum relaxation rule (***k=0***) of

the first order Raman spectrum. Serrano et al [55] used first-principles calculations based on density-functional theory to investigate the lattice dynamics of the three ZnO crystalline phases. For comparison purposes, the DOS data obtained by Serrano et al. [55] is inserted in Fig. 13, for one phonon $[\rho^1(\omega)]$, two sum phonon $[\rho^2_+(\omega)]$ and two subtract phonon$[\rho^2_-(\omega)]$, for the wurtzite phase. Comparing the shape of the Raman spectrum measured at 442 nm with the phonon DOS of $[\rho^1(\omega)]$, $[\rho^2_+(\omega)]$ and $[\rho^2_-(\omega)]$, it can be concluded that, apart from the asymmetry of the LO band, the Raman disorder activation of DOS does not represent the major Raman processes that occur in the ZnO film, indicating a good crystallinity of the sample. The asymmetry of the LO band towards lower Raman shift values can be explained by the momentum relaxation rule (***k***=**0**) of first order Raman spectrum due to the nanocrystalline nature of the sample. Nevertheless, and contrary to what would be expected under no incoming resonant excitation conditions [61], the LO mode is significantly more intense than the non-polar mode E_2 (high). Moreover, its overtone at about twice the LO frequency is detected at 1158 cm^{-1}. Both facts highlight the possibility of an outcoming resonant Raman process, which takes place when the energy of the scattered photon ($E_{s,photon}$= 2.73 eV) matches real electronic states. When the ZnO film is excited with 325 nm (3.81 eV) the Raman spectrum is dominated by the LO multiphonon and a photoluminescence tail is detected, which is related with the ZnO near band edge emission (NBE); as expected, when the laser energy is in resonance with an interband electronic transitions (incoming resonance). The multiphonon scattering process has been very scrutinized in ZnO, in either bulk [58,62], thin films [45] or nanostructures [46,47]. Using the ZnO absorption coefficient, α, reported by J.F Muth [63] the penetration depth (δ) attained in backscattering geometry $\left(\delta = {}^{1}/_{2\alpha}\right)$ is of ~ 31 nm and ~800 nm for the 325 nm and 442 nm HeCd laser lines, respectively. Thus, bearing in mind the difference in the penetration depth attained by changing the excitation wavelength from 325 nm to 442 nm, the experimental results show that, independent of the wavelength of excitation, the LO and 2LO are located at the same Raman shift values, meaning that the structure of ZnO film is very homogeneous in-depth up to 800 nm.

The same analysis is conducted for the doped ZnO films, samples ZnO:Bi (Fig. 13(b)) and ZnO:Ga (Fig. 13(c)). In the case of Bi-doping, the Raman spectrum measured with 442 nm and 325 nm laser lines closely matches the one obtained from the undoped ZnO sample in similar conditions. This fact indicates that if Bi atoms are incorporated in the ZnO wurtzite lattice, its level of doping is very low as the ZnO lattice dynamic remains the same, without presenting evidence of any additional disorder effect when compared with the ZnO sample. The peak position of the LO and 2LO coincides with the values obtained with the 442 nm laser line, showing the homogeneity of the ZnO:Bi film up to 800 nm.

For Ga-doping in ZnO (Fig. 13(c)), it is evident the importance of the disorder activation of the phonon DOS, specially one phonon DOS $[\rho^1(\omega)]$, in the Raman spectrum shape obtained upon excitation with the 442 nm laser line. With the introduction of Ga in ZnO lattice, the translational invariance of the crystal lattice is weakened and scattering events from the whole Brillouin zone are viable, making possible the participation of phonons from the entire Brillouin zone. Apart from the Raman peaks located at 439 cm^{-1} and 565 cm^{-1}, another peak at 277 cm^{-1} is clearly observed. The latter mode at 277 cm^{-1} registered

for the Ga-doped ZnO thin film sample has also been reported for Fe, Al, Ga [51], Sb [52] and N [53] doped films and is related with the disorder activation of the zone centre Raman forbidden B_1(low) mode [64] or a local vibrational mode in N implanted ZnO films [53]. However, since this mode has been detected for different type of dopants, its assignment to a local mode vibration seems less plausible. The peak at 439 cm^{-1} is located at the position expected for the zone centre ZnO E_2(high) mode, but the peak at 565 cm^{-1} has a lower frequency than the range of values expected for A_1 (LO) and E_1 (LO), if the angular dispersion of the LO quasi-mode above mentioned is considered. The non-polar E_2(high) mode involves mainly oxygen displacements in the plane perpendicular to the *c*-axis, while the quasi-LO modes involves both Zn and O displacements along *c*-axis. Thus, it is expected that the softening of the LO frequency might be related with the substitution of the Zn by the Ga atoms. Another aspect to point out is the huge difference observed in the Raman spectral shape when the laser line is changed for the UV line (325 nm). Under this experimental condition, a broadband with a maximum close to 500 cm^{-1} is observed and it is also evident a shoulder at about 1100 cm^{-1} with a rather small intensity, which appears on the tail of the luminescence, indicating Raman scattering under incoming resonance conditions. The broad Raman band at 500 cm^{-1} is between the LO and the E_2 (high) modes detected under off resonance conditions. The red shift is too high to be due to the effect of angular dispersion of the LO quasi-mode due to the nanocrystalline nature of the sample. Upon a more detailed inspection of the spectrum obtained with the 442 nm line in the spectral region between the LO and E_2 modes (high) it is verified that, contrary to the curve of the DOS [ρ^1 (ω)], the Raman intensity does not drop to zero close to 500 cm^{-1}, which may be due to the overlapping with the broadband at ~ 500 cm^{-1} detected with the 325 nm line. One explanation could be related with the compositional and in-depth strain inhomogeneity, only identified under incoming scattering resonant conditions. Another very strong hypothesis for this broad band could be due to a superposition of the LO mode and a Fröhlich-type vibrational mode that has been reported in resonant Raman scattering spectra of ZnO nanostructured layers [46], which participate in the multiphonon scattering as well. These Fröhlich-type vibrational modes are not present in bulk material, and have frequencies located in the frequency gap between TO and LO optical phonons. These specific frequencies are originated when the electromagnetic radiation propagates through nanostructures of polar materials, which results in electric dipole oscillations formed due the polarization of the nanostructure entities in the electric field of radiation [65]. The efficiency of Raman scattering caused by the Fröhlich-type vibrational modes (surface-related modes) is comparable with that of bulk LO and TO, only if the nanocrystalline diameters are less than 100 nm [65]. The spectra obtained with the 325 nm laser line for the ZnO:Ga film consists also of multiphonon resonant scattering superimposed on the photoluminescence tail, which in comparison to undoped ZnO and ZnO:Bi films is shifted to higher energies. This shift observed in the luminescence tail is a strong indication of the changes on the ZnO electronic bands as a result of Ga doping.

In the case of Ga, Bi-doping in ZnO (Fig. 13(d)), the measured μ-Raman spectra are very close to the obtained ones for the ZnO:Ga sample (Fig 13(c)). Compared to the ZnO:Ga sample, under 442 nm excitation, there is a slight deviation of the Raman bands towards lower frequencies and an enlargement of these bands, which is compatible with a slight increase in the degree of disorder. Furthermore, considering the experimental results

observed in the ZnO:Bi sample (Fig. 13(b)), it is very likely that these small differences are mainly associated with an increase of compositional disorder ascribed to the incorporation of Ga into the ZnO network.

4. Conclusions

The influence of Ga and Bi doping on the local structure of ZnO thin films was studied by several experimental techniques such as X-ray absorption spectroscopy, X-ray photoelectron spectroscopy, X-ray diffraction, transmission electron microscopy and Raman spectroscopy. It was found that the two dopants differently affect ZnO film structure. Small Ga^{3+} ions substitute zinc ions and introduce static disorder to the film structure, as is evidenced by the larger values of the MSRD σ^2(Zn-O) and σ^2(Zn-Zn) in Ga-doped ZnO films. On the contrary, large Bi^{3+} ions do not enter ZnO lattice, as verified from the similarity of the Bi L_3-edge EXAFS in the film and α-Bi_2O_3 powder, but are likely located in the disordered environment at the ZnO grain boundaries. Hence, the Bi-induced disorder does not have a prominent effect in hindering phonon propagation and on concomitantly decreasing thermal conductivity, as expected in a previous publication [13]. This conclusion is supported by energy-dispersive X-ray spectroscopy combined with TEM and Raman experiments. The fact that Bi ions do not substitute Zn ions in the wurtzite lattice enables the understanding on why in a previous report from the authors [13] the Seebeck coefficient of ZnO:Ga,Bi films actually decreases in absolute value from 40 $\mu V \cdot K^{-1}$ to 25 $\mu V \cdot K^{-1}$ with increase in Bi composition from 0.1 to 1.2 at. %, despite a decrease in electrical resistivity for these films in that Bi composition range. From XRD data it is concluded that all undoped and doped films crystallise in a ZnO phase with the hexagonal wurtzite crystal structure. Ga-doping decreases the relative diffraction peak intensity of (002) planes compared to the (100) and (101) planes, as already reported in the literature, without evidence of Ga_2O_3 phases. However, Bi doping and co-doping produces a greater effect, suggesting that Bi is not incorporated in the ZnO wurtzite cell, but segregates to the grain boundaries, mainly as Bi_2O_3 and small amount of Bi metal phases, which promotes a texturizing effect on the diffraction from the wurtzite phase. From high resolution electron microscopy it was verified that for the ZnO:Ga,Bi film the ZnO:Ga grains are delimited by Bi-enriched grain boundaries, providing further evidence that Bi is not incorporated in the ZnO wurtzite cell. From XPS analysis, no traces of Ga_2O_3 phases were discerned. Conversely, both Bi-metal and Bi_2O_3 binding energies were assigned from the Bi 4f core line analysis. The chemical composition was derived from the quantification analysis from XPS fits, where it was determined that the ZnO:Ga,Bi films are defective in oxygen content (46.1 at.%), arising primarily from oxygen vacancies, being the levels of Ga and Bi doping 2.2 and 1.6 at.%, respectively. The study of μ-Raman showed that the activation of the density of phonon states potentiated by structural/composition disorder is responsible for the Raman spectrum observed in Ga-doped ZnO films, corroborating the substitution of Zn by Ga. Contrarily, Bi-doped and undoped ZnO films reveal a similar crystalline lattice dynamic, confirming that Bi does not replace Ga in wurtzite cell. Moreover, Raman attest that chemical composition stated above is in-depth homogenous.

Acknowledgements

The experiment at HASYLAB/DESY was performed within the project I-20180036 EC. The research leading to this result has been supported by the project CALIPSOplus under the Grant Agreement 730872 from the EU Framework Programme for Research and Innovation HORIZON 2020. Filipe Correia is grateful to the *Fundação para a Ciência e Tecnologia* (FCT, Portugal) for the Ph.D. Grant SFRH/BD/111720/2015. Joana Ribeiro is grateful to the Project WinPSC - POCI-01-0247-FEDER-017796, for the research grant from the Agência Nacional de Inovação, co-funded by the European Regional Development Fund (ERDF), through the Operational Programme for Competitiveness and Internationalisation (COMPETE 2020), under the PORTUGAL 2020 Partnership Agreement. The authors acknowledge the funding from the Fundação para a Ciência e Tecnologia (FCT, Portugal) / PIDDAC through the Strategic Funds project reference UIDB/04650/2020-2023. Part of this work was developed within the scope of the project i3N, UIDB/50025/2020, financed by national funds through the FCT/MEC. Institute of Solid State Physics, University of Latvia as the Center of Excellence has received funding from the European Union's Horizon 2020 Framework Programme H2020-WIDESPREAD-01-2016-2017-TeamingPhase2 under grant agreement No. 739508, project CAMART2. The authors would like to thank the valuable help from Dr. Alec LaGrow and Dr. Dr. Alex Bondarchukat the International Iberian Nanotechnology Laboratory (INL), in Braga, Portugal, for the STEM/HRTEM experiments.

Data availability

The raw/processed data required to reproduce these findings cannot be shared at this time due to technical or time limitations.

References

[1] A. Janotti, C. Van Walle, Fundamentals of zinc oxide as a semiconductor, Reports Prog. Phys. 72 (2009) 126501. doi:10.1088/0034-4885/72/12/126501.

[2] Ü. Özgür, Y.I. Alivov, C. Liu, A. Teke, M.A. Reshchikov, S. Doğan, V. Avrutin, S.J. Cho, H. Morkoç, A comprehensive review of ZnO materials and devices, J. Appl. Phys. 98 (2005) 1–103. doi:10.1063/1.1992666.

[3] T. Tynell, M. Karppinen, Atomic layer deposition of ZnO: a review, Semicond. Sci. Technol. 29 (2014) 043001. doi:10.1088/0268-1242/29/4/043001.

[4] K. Ellmer, A. Bikowski, Intrinsic and extrinsic doping of ZnO and ZnO alloys, J. Phys. D. Appl. Phys. 49 (2016) 413002–413002. doi:10.1088/0022-3727/49/41/413002.

[5] H. Chen, Y. Liu, C. Xie, J. Wu, D. Zeng, Y. Liao, A comparative study on UV light activated porous TiO2and ZnO film sensors for gas sensing at room temperature, Ceram. Int. 38 (2012) 503–509. doi:10.1016/j.ceramint.2011.07.035.

[6] M. Al-Fandi, R. Oweis, B.A. Albiss, T. AlZoubi, M.-A. Al-Akhras, H. Qutaish, H. Khwailah, S. Al-Hattami, E. Al-Shawwa, A prototype Ultraviolet Light Sensor based on ZnO Nanoparticles/Graphene Oxide Nanocomposite Using Low Temperature Hydrothermal Method, IOP Conf. Ser. Mater. Sci. Eng. 92 (2015) 012009. doi:10.1088/1757-899X/92/1/012009.

[7] K.C. Lai, C.C. Liu, C. hsiung Lu, C.H. Yeh, M.P. Houng, Characterization of ZnO:Ga transparent contact electrodes for microcrystalline silicon thin film solar cells, Sol. Energy Mater. Sol. Cells. 94 (2010) 397–401. doi:10.1016/j.solmat.2009.12.002.

[8] C.G. Granqvist, Transparent conductors as solar energy materials: A panoramic review, Sol. Energy Mater. Sol. Cells. 91 (2007) 1529–1598. doi:10.1016/j.solmat.2007.04.031.

[9] T.J. Coutts, D.L. Young, X. Li, Characterization of transparent conducting oxides, MRS Bull. 25 (2000) 58.

[10] P. Jood, R.J. Mehta, Y. Zhang, T. Borca-Tasciuc, S.X. Dou, D.J. Singh, G. Ramanath, Heavy element doping for enhancing thermoelectric properties of nanostructured zinc oxide, RSC Adv. 4 (2014) 6363. doi:10.1039/c3ra46813e.

[11] G. Ren, J. Lan, C. Zeng, Y. Liu, B. Zhan, S. Butt, Y.H. Lin, C.W. Nan, High Performance Oxides-Based Thermoelectric Materials, Jom. 67 (2015) 211–221. doi:10.1007/s11837-014-1218-2.

[12] S. Saini, P. Mele, H. Honda, T. Suzuki, K. Matsumoto, K. Miyazaki, A. Ichinose, L. Molina Luna, R. Carlini, A. Tiwari, L.M. Luna, R. Carlini, A. Tiwari, Effect of self-grown seed layer on thermoelectric properties of ZnO thin films, Thin Solid Films. 605 (2015) 289–294. doi:10.1016/j.tsf.2015.09.060.

[13] F.C. Correia, P.B. Salvador, J.M. Ribeiro, A. Mendes, C.J. Tavares, Effect on the electrical and morphological properties of Bi incorporation into ZnO:Ga and ZnO:Al thin films deposited by confocal magnetron sputtering, Vacuum. 152 (2018) 252–260. doi:10.1016/j.vacuum.2018.03.033.

[14] H.Y. Liu, V. Avrutin, N. Izyumskaya, Ü. Özgür, A.B. Yankovich, A. V. Kvit, P.M. Voyles, H. Morkoç, Electron scattering mechanisms in GZO films grown on a-sapphire substrates by plasma-enhanced molecular beam epitaxy, J. Appl. Phys. 111 (2012) 103713. doi:10.1063/1.4720456.

[15] F. Chouikh, Y. Beggah, M.S. Aida, Optical and electrical properties of Bi doped ZnO thin films deposited by ultrasonic spray pyrolysis, J. Mater. Sci. Mater. Electron. 22 (2011) 499–505. doi:10.1007/s10854-010-0167-y.

[16] J.M. Ribeiro, F.C. Correia, P.B. Salvador, L. Rebouta, L.C. Alves, E. Alves, N.P. Barradas, A. Mendes, C.J. Tavares, Compositional analysis by RBS, XPS and EDX of ZnO:Al,Bi and ZnO:Ga,Bi thin films deposited by d.c. magnetron sputtering, Vacuum. 161 (2019) 268–275. doi:10.1016/j.vacuum.2018.12.038.

[17] J.M. Ribeiro, F.C. Correia, A. Kuzmin, I. Jonane, M. Kong, A.R. Goñi, J.S. Reparaz, A. Kalinko, E. Welter, C.J. Tavares, Influence of Nb-doping on the local structure and thermoelectric properties of transparent TiO2:Nb thin films, J. Alloys Compd. 838 (2020) 155561. doi:10.1016/j.jallcom.2020.155561.

[18] E. Welter, R. Chernikov, M. Herrmann, R. Nemausat, A beamline for bulk sample x-ray absorption spectroscopy at the high brilliance storage ring PETRA III, AIP Conf. Proc. 2054 (2019) 1–6. doi:10.1063/1.5084603.

[19] A. Kuzmin, J. Chaboy, EXAFS and XANES analysis of oxides at the nanoscale, IUCrJ. 1 (2014) 571–589. doi:10.1107/S2052252514021101.

[20] A.L. Ankudinov, B. Ravel, J.J. Rehr, S.D. Conradson, Real-space multiple-scattering calculation and interpretation of x-ray-absorption near-edge structure, Phys. Rev. B. 58 (1998) 7565–7576. doi:10.1103/PhysRevB.58.7565.

[21] J.J. Rehr, R.C. Albers, Theoretical approaches to x-ray absorption fine structure, Rev. Mod. Phys. 72 (2000) 621–654. doi:10.1103/RevModPhys.72.621.

[22] L. Hedin, B.I. Lundqvist, Explicit local exchange-correlation potentials, J. Phys. C Solid State Phys. 4 (1971) 2064–2083. doi:10.1088/0022-3719/4/14/022.

[23] H. Karzel, W. Potzel, M. Köfferlein, W. Schiessl, M. Steiner, U. Hiller, G. Kalvius, D. Mitchell, T. Das, Lattice dynamics and hyperfine interactions in ZnO and ZnSe at high external pressures, Phys. Rev. B - Condens. Matter Mater. Phys. 53 (1996) 11425–11438. doi:10.1103/PhysRevB.53.11425.

[24] J. Åhman, G. Svensson, J. Albertsson, A reinvestigation of β-gallium oxide, Acta Crystallogr. Sect. C Cryst. Struct. Commun. 52 (1996) 1336–1338. doi:10.1107/S0108270195016404.

[25] R.D. Shannon, Revised effective ionic radii and systematic studies of interatomic distances in halides and chalcogenides, Acta Crystallogr. Sect. A. 32 (1976) 751–767. doi:10.1107/S0567739476001551.

[26] Y. Joly, X-ray absorption near-edge structure calculations beyond the muffin-tin approximation, Phys. Rev. B - Condens. Matter Mater. Phys. 63 (2001). doi:10.1103/PhysRevB.63.125120.

[27] O. Bunău, Y. Joly, Self-consistent aspects of x-ray absorption calculations, J. Phys. Condens. Matter. 21 (2009) 345501. doi:10.1088/0953-8984/21/34/345501.

[28] O. Keski-Rahkonen, M.O. Krause, Total and partial atomic-level widths, At. Data Nucl. Data Tables. 14 (1974) 139–146. doi:10.1016/S0092-640X(74)80020-3.

[29] S.A. Ivanov, R. Tellgren, H. Rundlöf, V.G. Orlov, Structural studies of α-Bi_2O_3 by neutron powder diffraction, Powder Diffr. 16 (2001) 227–230. doi:10.1154/1.1401200.

[30] A.A. Mistonov, A.P. Chumakov, R.P. Ermakov, L.D. Iskhakova, A. V. Zakharova, A. V. Chumakova, K.O. Kvashnina, Electronic structure studies of bismuth compounds using high energy resolution X-ray spectroscopy and ab initio calculations, J. Alloys Compd. 753 (2018) 646–654. doi:10.1016/j.jallcom.2018.04.190.

[31] C. Xu, J. Chun, D.E. Kim, J.J. Kim, B. Chon, T. Joo, Electrical properties and near band edge emission of Bi-doped ZnO nanowires, Appl. Phys. Lett. 90 (2007) 083113. doi:10.1063/1.2431715.

[32] P. Jood, R.J. Mehta, Y. Zhang, T. Borca-Tasciuc, S.X. Dou, D.J. Singh, G. Ramanath, Heavy element doping for enhancing thermoelectric properties of nanostructured zinc oxide, RSC Adv. 4 (2014) 6363–6368. doi:10.1039/c3ra46813e.

[33] W. Guan, L. Zhang, C. Wang, Y. Wang, Theoretical and experimental investigations of the thermoelectric properties of Al-, Bi- and Sn-doped ZnO, Mater. Sci. Semicond. Process. 66 (2017) 247–252. doi:10.1016/j.mssp.2017.03.027.

[34] J. Hu, R.G. Gordon, Atmospheric pressure chemical vapor deposition of gallium doped zinc oxide thin films from diethyl zinc, water, and triethyl gallium, J. Appl. Phys. 72 (1992) 5381–5392. doi:10.1063/1.351977.

[35] P. Krongarrom, S.T. Rattanachan, T. Fangsuwannarak, Structural and optical characterizations of n-type doped ZnO by sol-gel method for photovoltaic, ECTI-CON 2011 - 8th Electr. Eng. Electron. Comput. Telecommun. Inf. Technol. Assoc. Thail. - Conf. 2011. (2011) 50–53. doi:10.1109/ECTICON.2011.5947768.

[36] Z. Zhou, J. Yang, Q. Jiang, Y. Luo, D. Zhang, Y. Ren, X. He, J. Xin, Multiple effects of Bi doping in enhancing the thermoelectric properties of SnTe, J. Mater. Chem. A. 4 (2016) 13171–13175. doi:10.1039/c6ta04240f.

[37] Z. Zhou, J. Yang, Q. Jiang, X. Lin, J. Xin, A. Basit, J. Hou, B. Sun, Enhanced thermoelectric performance of SnTe: High efficient cation - anion Co-doping, hierarchical microstructure and electro-acoustic decoupling, Nano Energy. 47 (2018) 81–88. doi:10.1016/j.nanoen.2018.02.045.

[38] G. Schon, Elsevier Scientific Publishing, J. Electron Spectros. Relat. Phenomena. 2 (1973) 75–86. doi:10.1016/0006-8993(75)90185-7.

[39] Thermo Scientific XPS, XPS Ref. Table Elem. (2018). https://xpssimplified.com/elements/zinc.php (accessed December 21, 2018).

[40] M.C. Biesinger, L.W.M. Lau, A.R. Gerson, R.S.C. Smart, Resolving surface chemical states in XPS analysis of first row transition metals, oxides and hydroxides: Sc, Ti, V, Cu and Zn, Appl. Surf. Sci. 257 (2010) 887–898.

doi:10.1016/j.apsusc.2010.07.086.

[41] F.C. Correia, N. Bundaleski, O.M.N.D. Teodoro, M.R. Correia, L. Rebouta, A. Mendes, C.J. Tavares, XPS analysis of ZnO:Ga films deposited by magnetron sputtering: Substrate bias effect, Appl. Surf. Sci. 458 (2018) 1043–1049. doi:10.1016/j.apsusc.2018.07.135.

[42] M.C. Biesinger, B.P. Payne, A.P. Grosvenor, L.W.M. Lau, A.R. Gerson, R.S.C. Smart, Resolving surface chemical states in XPS analysis of first row transition metals, oxides and hydroxides: Cr, Mn, Fe, Co and Ni, Appl. Surf. Sci. 257 (2011) 2717–2730. doi:10.1016/j.apsusc.2010.10.051.

[43] M.V. Castro, C.J. Tavares, Dependence of Ga-doped ZnO thin film properties on different sputtering process parameters: Substrate temperature, sputtering pressure and bias voltage, Thin Solid Films. 586 (2015) 13–21. doi:10.1016/j.tsf.2015.04.036.

[44] F.C. Correia, J.M. Ribeiro, P.B. Salvador, A. Welle, M. Bruns, A. Mendes, C.J. Tavares, Combined in-depth X-ray Photoelectron Spectroscopy and Time-of-Flight Secondary Ion Mass Spectroscopy study of the effect of deposition pressure and substrate bias on the electrical properties and composition of Ga-doped ZnO thin films grown by magnetron , Thin Solid Films. 665 (2018) 184–192. doi:10.1016/j.tsf.2018.09.004.

[45] M.F. Cerqueira, M.I. Vasilevskiy, F. Oliveira, a G. Rolo, T. Viseu, J. Ayres de Campos, E. Alves, R. Correia, Resonant Raman scattering in ZnO:Mn and ZnO:Mn:Al thin films grown by RF sputtering., J. Phys. Condens. Matter. 23 (2011) 334205. doi:10.1088/0953-8984/23/33/334205.

[46] V. V. Ursaki, I.M. Tiginyanu, V. V. Zalamai, E. V. Rusu, G.A. Emelchenko, V.M. Masalov, E.N. Samarov, Multiphonon resonant Raman scattering in ZnO crystals and nanostructured layers, Phys. Rev. B. 70 (2004) 155204. doi:10.1103/PhysRevB.70.155204.

[47] H.M. Cheng, K.F. Lin, H.C. Hsu, W.F. Hsieh, Size dependence of photoluminescence and resonant Raman scattering from ZnO quantum dots, Appl. Phys. Lett. (2006). doi:10.1063/1.2217925.

[48] H.F. Liu, S. Tripathy, G.X. Hu, H. Gong, Surface optical phonon and A1 (LO) in ZnO submicron crystals probed by Raman scattering: Effects of morphology and dielectric coating, J. Appl. Phys. (2009). doi:10.1063/1.3087482.

[49] Z. Mao, C. Fu, X. Pan, X. Chen, H. He, W. Wang, Y. Zeng, Z. Ye, Raman-based measurement of carrier concentration in n-type ZnO thin films under resonant conditions, Phys. Lett. Sect. A Gen. At. Solid State Phys. (2020). doi:10.1016/j.physleta.2019.126148.

[50] C. Lung, M. Toma, M. Pop, D. Marconi, A. Pop, Characterization of the structural and optical properties of ZnO thin films doped with Ga, Al and (Al+Ga), J. Alloys Compd. (2017). doi:10.1016/j.jallcom.2017.07.265.

[51] C. Bundesmann, N. Ashkenov, M. Schubert, D. Spemann, T. Butz, E.M. Kaidashev, M. Lorenz, M. Grundmann, Raman scattering in ZnO thin films doped with Fe, Sb, Al, Ga, and Li, Appl. Phys. Lett. (2003). doi:10.1063/1.1609251.

[52] K. Samanta, P. Bhattacharya, R.S. Katiyar, Raman scattering studies of p-type Sb-doped ZnO thin films, J. Appl. Phys. (2010). doi:10.1063/1.3516493.

[53] F. Reuss, C. Kirchner, T. Gruber, R. Kling, S. Maschek, W. Limmer, A. Waag, P. Ziemann, Optical investigations on the annealing behavior of gallium- and nitrogen-implanted ZnO, J. Appl. Phys. (2004). doi:10.1063/1.1650899.

[54] J. Serrano, F.J. Manjón, A.H. Romero, F. Widulle, R. Lauck, M. Cardona, Dispersive phonon linewidths: The E2 phonons of ZnO, Phys. Rev. Lett. (2003). doi:10.1103/physrevlett.90.055510.

[55] R. Cuscó, E. Alarcón-Lladó, J. Ibáñez, L. Artús, J. Jiménez, B. Wang, M.J. Callahan, Temperature dependence of Raman scattering in ZnO, Phys. Rev. B - Condens. Matter Mater. Phys. (2007). doi:10.1103/PhysRevB.75.165202.

[56] N. Ashkenov, B.N. Mbenkum, C. Bundesmann, V. Riede, M. Lorenz, D. Spemann, E.M. Kaidashev, A. Kasic, M. Schubert, M. Grundmann, G. Wagner, H. Neumann, V. Darakchieva, H. Arwin, B. Monemar, Infrared dielectric functions and phonon modes of high-quality ZnO films, J. Appl. Phys. (2003). doi:10.1063/1.1526935.

[57] T. Sander, S. Eisermann, B.K. Meyer, P.J. Klar, Raman tensor elements of wurtzite ZnO, Phys. Rev. B - Condens. Matter Mater. Phys. (2012). doi:10.1103/PhysRevB.85.165208.

[58] J.M. Calleja, M. Cardona, Resonant Raman scattering in ZnO, Phys. Rev. B. (1977). doi:10.1103/PhysRevB.16.3753.

[59] R. Loudon, The Raman effect in crystals, Adv. Phys. (1964). doi:10.1080/00018736400101051.

[60] J. Serrano, A.H. Romero, F.J. Manjón, R. Lauck, M. Cardona, A. Rubio, Pressure dependence of the lattice dynamics of ZnO: An ab initio approach, Phys. Rev. B. 69 (2004) 094306. doi:10.1103/PhysRevB.69.094306.

[61] R. Cuscó, E. Alarcón-Lladó, J. Ibanez, L. Artús, J. Jiménez, B. Wang, M.J. Callahan, Temperature dependence of Raman scattering in ZnO, Phys Rev B. 75 (2007) 165202. doi:10.1103/PhysRevB.75.165202.

[62] J.F. Scott, Uv resonant Raman scattering in ZnO, Phys. Rev. B. (1970). doi:10.1103/PhysRevB.2.1209.

[63] J.F. Muth, R.M. Kolbas, A.K. Sharma, S. Oktyabrsky, J. Narayan, Excitonic structure and absorption coefficient measurements of ZnO single crystal epitaxial films deposited by pulsed laser deposition, J. Appl. Phys. (1999). doi:10.1063/1.370601.

[64] J. Serrano, F.J. Manjón, A.H. Romero, A. Ivanov, M. Cardona, R. Lauck, A. Bosak, M. Krisch, Phonon dispersion relations of zinc oxide: Inelastic neutron scattering and ab initio calculations, Phys. Rev. B. 81 (2010) 174304. doi:10.1103/PhysRevB.81.174304.

[65] R. Ruppin, R. Englman, Optical phonons of small crystals, Reports Prog. Phys. 33 (1970) 304. doi:10.1088/0034-4885/33/1/304.